

State-selective Production of Oxygen Molecular Ions for New Physics Searches

Alexander Frenett

Advisor: Professor David A. Hanneke
April 30, 2018

Submitted to the
Department of Physics & Astronomy of Amherst College
in partial fulfilment of the
requirements for the degree of
Bachelors of Arts with honors

© 2018 Alexander Frenett

APPENDIX A

COVER SHEET TO BE APPENDED TO ALL THESES

By law, copyright in your thesis belongs to you, the author, including all rights of publication and reproduction. Only the copyright holder may determine what others may do with the thesis.

STEP 1. What should the library do with your thesis? (Choose one)



Share my thesis

You authorize the library to share your thesis with others according to the Creative Commons license selected in step 2. (See Appendix B for an explanation of the three options.)



Place an optional embargo on my thesis

The library should not allow anybody except college officials to see its copy of my thesis until January 1st of the year _____. (e.g., 1 year=2018, 5 years=2022, 100 years=2117)

Under this option, you ask the library to prevent anyone else from accessing its copy of your thesis. At the end of the lockdown period, the library will distribute its copy of your thesis according to the license you choose below. (See Appendix B for an explanation of the three options.)

STEP 2. Select a license for your thesis. (Choose one)

CC BY-NC-ND

CC BY-NC-SA

CC BY

The type of Creative Commons license you choose determines what others may and may not do with your thesis. (See Appendix B for an explanation of the three options.)

STEP 3. Sign.

Please note that, by choosing to make your thesis available (whether now or at a future date), you are waiving any protections of the Family Educational Rights and Privacy Act (FERPA) that may apply with respect to your thesis as of the date specified. FERPA generally restricts disclosure by the college of records related to your education.

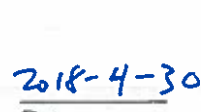

Student Signature


Student Name


Date


Thesis Advisor Signature


Thesis Advisor Name


Date

Abstract

The Standard Model (SM) merges quantum mechanics and special relativity to accurately and precisely describe nearly all physics we observe in the universe. However, it is famously unable to explain some observed phenomena, like gravity and dark matter. Accordingly, many theorists have extended the SM to explain more of nature. A major goal in experimental physics is to observe the “new physics” that is predicted by these extensions. While many pursuits of such “new physics” are done in colliders and accelerators, there is a complementary realm of experiments that seek to measure effects that the theories have on atomic and molecular systems. Of particular note for these small-scale projects, SM extensions often predict that some fundamental constants may change over time. In the tradition of this type of experiment, we have proposed to explore the potential temporal variation of the proton-to-electron mass ratio ($\dot{\mu}/\mu$) by tracking the stability of a clock transition between two vibrational states in molecular oxygen ions. To do so, we require a source of O_2^+ ions in their rovibrational ground state. Electron-beam ionization does not provide the necessary state-selectivity, and so we seek to use (2+1) resonance-enhanced multi-photon ionization (REMPI) to create the ions.

In this thesis, I first describe the proposed experimental methods to measure $\dot{\mu}/\mu$. I then relate the basic theory that describes the REMPI process we seek to use. Finally, using both the REMPI theory and experimental needs for the $\dot{\mu}/\mu$ measurement, I explain how and why we designed and constructed a test chamber to realize the ionization. This chamber consists of three main parts: a supersonic oxygen beam to produce a cold and dense set of neutral molecules; an ionization region, where the ionizing pulsed laser and molecular beam cross; and a simple time-of-flight setup to measure the yield of ions produced. In the work, we demonstrate production of a molecular beam and control over the pulsed laser tuning, describe future experiments we will do using both beams, and discuss longer term plans for integrating the beam and time-of-flight apparatus into our ion trapping chamber.

Acknowledgments

First and foremost I would like to thank Professor Hanneke for his invaluable assistance and guidance. Though I can say this thesis would have been impossible without him, and that would be true, this would fail to sum up the impact he has had on my Amherst experience. Not only has he made this project possible, he is the one that fostered my ability to attempt such a feat in the first place. For the completion of this work and my success in physics more generally, I am infinitely indebted to his mentorship and patience throughout my time working with him over the past three years.

I would next like to thank Ryan Carollo for the knowledge he brought to the table on almost every topic we grappled with. His experience and ability were crucial to efficiently building and constructing the apparatus. Without the time and effort he devoted to this project, we would never have gotten to the point we did.

Special thanks to Jim Kubasek for making us what seemed like a new part every week, all the while maintaining his usual contagiously friendly attitude. This project would have been impossible if not for his incredible machining ability. Thanks also to Brian Crepeau for looking over many circuit diagrams, fixing many boards, and generally ensuring that our electronics continue to work.

To my fellow physics majors, I owe you so much for my experience here these past four years. I appreciate all the help on problem sets and have cherished the social atmosphere we've developed.

To Kaeli, thank you for being there for me in many ways since even before we got

here. My time here would have been unimaginably different without you.

Finally, I cannot explain how extremely grateful I am to my family for their support these past four years. For the many visits, phone calls, emails, and of course snacks: thank you.

This material is based upon work supported by the Amherst College Dean of the Faculty and by the National Science Foundation under CAREER grant number PHY-1255170.

Contents

1	Introduction	1
1.1	Measuring Time	1
1.2	Selective State Creation of Ionic Oxygen	3
1.3	Ionization in the Lab	7
1.4	Chamber Characterization	14
1.5	Future Plans	15
1.6	A Note	17
2	Overview and Motivation	18
2.1	Measurement of $\dot{\mu}/\mu$	19
2.2	Current Status and Projects	25
3	Photoionization Theory	29
3.1	Overview	30
3.2	Neutral Excitation	32
3.3	Ionization	37
4	Design and Construction of the Test Chamber	43
4.1	The Oxygen Beam	44
4.1.1	Molecular Beams	44
4.1.2	Realizing a Beam	50
4.2	The Ionization Chamber	57
4.2.1	Chamber Design	57
4.2.2	The Realized Ionization Chamber	61
4.3	Ion Detection	63
4.3.1	Detection Method	63
4.3.2	Building the Ion Detector	69
4.4	Regroup	76
5	Characterizing the Chamber and Instruments	77
5.1	Initial Pumpdown	78
5.2	First Gas Pulses	81
5.3	Starting Up the MCP	85
5.4	Triggering	88
5.5	Fully Operational	90

6	Conclusion and Future Plans	92
6.1	Short-Term	92
6.2	Longer-Term	94
A	More Ionization Theory	97

List of Figures

1.1	Schematic of a simple photoionization process	4
1.2	Basic scheme of oxygen (2+1) REMPI	6
1.3	Block diagram of the test chamber	9
1.4	CAD images of the full test chamber	10
1.5	Photographs of the assembled chamber	12
2.1	Photograph of trapped Be^+ and O_2^+ ions	22
2.2	O_2^+ $v = 0 - 11$ vibrational excitation plot	24
2.3	O_2^+ dissociation plot	28
3.1	Detailed plot of (2+1) oxygen REMPI	31
3.2	Rotational spectra of the $\text{O}_2 X^3\Sigma_g^- \rightarrow d^1\Pi_g$ Excitation	36
4.1	Characteristics of a free jet	46
4.2	Relative positions of the quitting surface, skimmer, and Mach disk	47
4.3	CAD images of the beam creation chamber	51
4.4	Photograph of the pulsed valve	52
4.5	Valve pulsing circuit	53
4.6	Pressure decay from a single pulse	55
4.7	Dimensions and profile of the skimmer	56
4.8	Photographs of the skimmer assembly	57
4.9	CAD images of the ionization chamber	62
4.10	SIMION ion detection simulations	68
4.11	Design of the electrodes	70
4.12	Photograph of the electrode assembly	73
4.13	Photographs of the chamber-mounted electrode assembly	74
4.14	Circuit diagram of the voltage divider to power the MCP	75
4.15	Photographs of the MCP assembly	76
5.1	Pressure drop during the initial chamber pumpdown	80
5.2	Profile of the pressure of a single gas pulse	82
5.3	Effects of gas pulsing frequency on background pressure	83
5.4	Pressure plots showing problems with the ion gauge controllers	85
5.5	Plot of pressure changes due to different lengths of gas pulse	86
5.6	MCP “dark count” height distribution	87
5.7	MCP “dark count” time-integration distribution	87

5.8	Time ordering of the pulse valve triggering, laser triggering, and laser firing pulses	91
-----	--	----

Chapter 1

Introduction

1.1 Measuring Time

Measuring time has been a human preoccupation for millenia because quantifying time is a prerequisite to accurately describing *change*. The units that were chosen and created were not arbitrary, but always based on something supposedly concrete; some property that seems *not* to change with time. After all, only by reference to the immutable does change make any sense. Hence the original definition of day from the sun, of year from the seasons [1]. Over centuries, humans have discovered that these natural phenomena are not as invariable as they may seem. In face of these discoveries, some made new references for time. In ancient Egypt and China, they found that they could engineer the rate of water falling to be remarkably constant, and they created clocks based on that principle in centuries or millenia B.C.E [1]. The complexity of the water clocks varied greatly, from simple jars with a steady drip to elaborate structures that used falling water to turn wheels and ring bells at specific intervals. Still more precise mechanical clocks arose in the middle ages. Originally also powered by falling water, they were soon replaced by clocks which counted oscillations of some sort: usually of spring or a pendulum [1]. The properties

of these oscillators were improved over centuries with electromechanical oscillators and very large pendula. The advancement of the physical sciences in the late 1800s both necessitated and created new, and better, clocks. With frequent measurement of sub-second and sub-millisecond phenomena in scientific and technical fields, even the improved mechanical clocks were too imprecise and inaccurate to satisfactorily use in many experiments.

Along with the discovery of oscillatory properties of natural materials came their use as better time sources: oscillations in quartz were first observed in the late 1800s, and this discovery was quickly followed by the creation of the crystal oscillator in the early 20th century [1]. Moving to driven natural oscillators instead of man-made ones shrank irregularities in the timekeeping and improved both precision and stability. However, this standard would not suffice for long with the explosion of physics in the 1900s into the quantum mechanical and relativistic realms, which required even higher precision. The detection of new particles, and the characterization of light and matter interaction, both necessitated and allowed the creation of atomic clocks [1]. Instead of with a pendulum, spring, or electrified crystal, we now define “the second” as a number of oscillations of the radiation that is emitted from a microwave transition in cesium. In recent years, groups have created clocks that work with transitions in the visible range, allowing even more stability by cutting down on the experimental uncertainty [2].

While atomic optical clocks will likely continue to dominate the realm of temporal standards in the near future, in the Hanneke lab we work towards developing clocks that use molecular, instead of atomic, transitions. Specifically, in our case, a transition between the $v = 0 - 11$ vibrational states in trapped singly-ionized molecular oxygen, O_2^+ . Molecules show promise as future clock candidates because of the relative complexity of their energy structure, which provides a larger number of optically accessible narrow-linewidth (low natural uncertainty) transitions than in atomic

systems. Measuring one of these precisely-defined transitions in O_2^+ with technology already developed for optical atomic clocks will help us push forward the limits of timekeeping by testing the feasibility of optical molecular clocks as a future standard.

In addition to using this frequency measurement as a clock source, we also wish to use it as a probe of fundamental physics. In the last decade, physicists have verified still more of both the Standard Model, with the discovery of the Higgs boson[3, 4], and Einstein’s general relativity, with the observation of gravitational waves[5]. Nevertheless, the universe continues to hold various mysteries: dark matter, the matter/anti-matter disparity, and many other phenomena are all but confirmed to exist, and yet no adequate theoretical descriptions have been experimentally verified. Some possible explanations of these observations predict time-variation of some fundamental constants[6, 7]. One such constant is the proton-to-electron mass ratio $m_p/m_e = \mu$ [6, 7]. Since vibrational levels in molecules are sensitive to this ratio[8], measurement of the stability of the vibrational transition probes this prediction. If the frequency is not stable over time, the measurement will be evidence of time variation of μ . Even if the frequency does not change, the stability measurement can be interpreted to put tighter limits on the magnitude of possible variation. My work in this thesis serves an integral role in making these measurements possible. To drive the desired $v = 0 - 11$ vibrational transition in the ion, we of course require $v = 0$ state ions, preferably in their ground rotational state. In addition, we will require a way to confirm the existence of these ions. This project makes progress on both the creation of vibrational ground state oxygen ions and methods to detect them.

1.2 Selective State Creation of Ionic Oxygen

To create ions in the vibrational ground state, we will *photoionize* oxygen molecules out of their respective ground state. Photoionization (PI) is a process through which

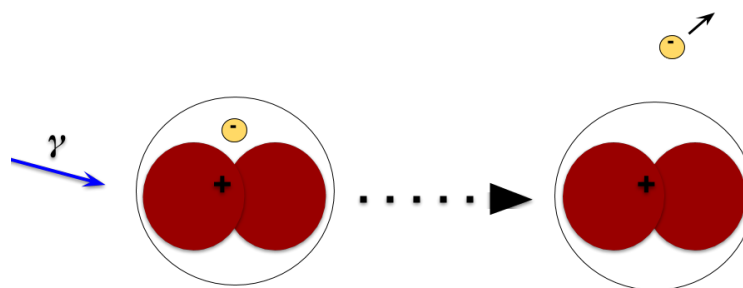


Figure 1.1: Depiction of a simple photoionization event. Incident light γ is absorbed by a diatomic molecule, exciting it to an extent that the electron is separated from the ionic core.

molecules or atoms are excited via absorption of a photon to the ionization continuum, depicted simply in Fig. 1.1. To explain the process briefly, it helps to treat the ionic core and valence electron as a oscillator-like quantum system with an energy well due to the Coulomb interaction [9]. It is then evident that if the electron is given sufficient energy, the system will no longer stay in a bound state; the electron will separate from the ionic core.

We favor this mechanism over other means of ionization because of the precision the method provides. Whereas electron beam ionization, a process in which ionization occurs because of electron-beam bombardment of the target atom or molecule, will certainly create ions, the energy resolution is too low to guarantee vibrational state-selectivity. In such a process, the energy given to the target molecules is variable, and so too is the internal and external energy of the resulting ions. On the other hand, the energy resolution of a laser is extremely high. Frequently, the precision of a photoionization process is not limited by the resolution of the laser, but by the natural linewidth of the transition. This process can even be used for rotational-state selectivity, which requires significantly smaller linewidth than only vibrational selectivity.

As each species of atom or molecule has a different structure, there is no *single* photoionization process; there are many, to the point that overarching characterization is not especially enlightening. Investigation of the specific process we use is more useful. In oxygen, there is a well-known process called (2+1) resonance-enhanced multiphoton ionization (REMPI) that produces ions in the $X\ ^2\Pi_g$ ionic ground state from the $X\ ^3\Sigma_g^-$ neutral ground state¹[11, 12]. This process is not a one-photon excitation to the continuum, as the simplest PIs are. Instead, the neutral molecule is first excited to an intermediate state in the neutral molecule ($d\ ^1\Pi_g$) via a two-photon excitation (a resonant absorption). Then, a third photon excites the intermediate state to the continuum. The order and role of these three photons is described by the “2+1” label. The energy between the ground and intermediate neutral states requires two 300 nm photons for the excitation, and the ionization itself requires a photon of 325 nm or shorter. A simple schematic illustrating the (2+1) REMPI process we will use for oxygen can be found in Fig. 1.2.

These photon energies are approximate because they fail to take into account rotational structure of the molecule. As a diatomic molecule, oxygen has rotational degrees of freedom around two axes [9]. The amount of energy held in these degrees of freedom in the initial molecule and final ion does affect the excitation and ionization energies. Though vibrational state affects our later project much more than rotational state, we do desire the ground rotational state ion if possible. This structure is thus important to us, though still small compared to the other energies involved. Thanks to the similar energies of the excitation and ionization photons, both processes *can* be done with a single laser at the higher frequency. However, if this route is taken, though vibrational selectivity should be guaranteed, absolute rotational selectivity

¹Molecular term symbols can be interpreted in a similar way to atomic term symbols. As a quick reference, the English letters label the states as ground or excited states (X is ground, other letters are various excited states), and the capital Greek letter tells the projection of the orbital angular momentum along the internuclear axis. The superscript number is related to the total electronic spin quantum number, and the subscript letter describes a nuclear symmetry. For a more complete discussion, see Chapter 3, or Brown and Carrington 26, 197-203 [10].

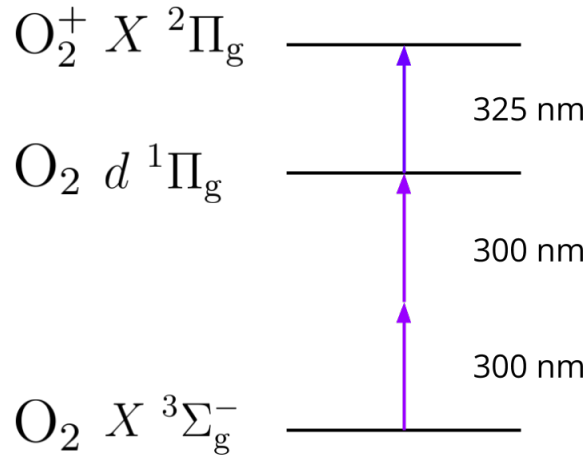


Figure 1.2: Schematic showing the relevant energy levels for the (2+1) REMPI process and how they are connected via the excitation and ionization lasers. Two 300 nm photons from the excitation laser are used to excite the oxygen molecule, and a single 325 nm or shorter photon does the actual ionization.

will not be possible due to the complications introduced by the additional structure, as discussed in Chapter 3.

The general rules for photoionization are based primarily on angular momentum conservation. However, due to the extra angular momenta in a molecule, the various couplings can make the process tricky to understand. To begin an explanation, it is first important to note that the neutral oxygen molecule ground state, $X^3\Sigma_g^-$, is a hyperfine triplet. From there, we can bring in a principle taught in introductory quantum mechanics: the absorption of a single photon by an atom or molecule can change the total angular momentum J by ± 1 units. Since the excitation here is a two-photon process, the allowed changes in angular momentum between the neutral $X^3\Sigma_g^-$ and $d^1\Pi_g$ states are $\Delta J = \pm 0, 2$ [13]. It turns out to be useful to use $N = J - S$, where S is the electronic spin quantum number, as a good quantum number for the excitation instead of J . This means that, for the triplet ground state, N states are defined by $N = J, J \pm 1$. As a result of these two observations, we see that

from a single ground state, there can be *seven* possible excited N' states, since ΔN can be $\pm 0, 1, 2, 3$ [13]. Like the excitation, the ionization process also changes the angular momentum, although determining how so requires deeper analysis because the ionizing electron *does* change the spin and can remove additional orbital angular momentum from the system [14]. For further discussion of both of these processes and how we obtain some state-selectivity through them, see Chapter 3 and Appendix A. For now, this overview of the (2+1) REMPI process provides enough information to see that the rotational structure of the molecule is complicated enough that obtaining state-selectivity through this process is not trivial.

1.3 Ionization in the Lab

Having a theoretical understanding of the (2+1) REMPI process does not provide a means for actually creating the ions in the lab. It is here that the majority of my work on this thesis comes in. There are actually relatively few requirements the theory places on laboratory realization, besides the laser frequency. Because the excitation transition is a two-photon process, we require a lot of intensity if we want to drive it with any significant probability[15]. As such, we use a pulsed laser because it is able to deliver more instantaneous power than similar-sized or cost continuous-wave (CW) lasers. Specifically, we use a Nd:YAG-pumped pulsed dye laser, which is passed through a doubling cavity to produce the necessary UV light around 300 nm.

Though this laser is necessitated by the particularities of the REMPI process, other properties, like the density or volume of the oxygen in the experiment, ought not to change the ionization process so long as they do not create new phenomena. As such, a device capable of testing (2+1) REMPI on molecular oxygen in our lab can take advantage of techniques and technologies to make the process easier and more useful for the later oxygen transition measurement. Most notably, making the components

compatible with conditions that will be found in the final experiment means keeping the main chamber, where the ionization actually occurs, able to function at ultra-high vacuum² (UHV). This requirement provides basic external limitations on items we use in the apparatus (such as choice of chamber strength and the material of instruments). A major part of this thesis was designing a test chamber with these restrictions that could still demonstrate the physics we want to observe in an easy and controllable manner. The chamber we created can be conceptually broken into three interacting parts/regions, illustrated in a block diagram in Fig. 1.3. We begin with a beam of neutral oxygen molecules. A conical skimmer then separates out the cold center of this beam, which passes into a region where the excitation and ionization light intersects the beam. Finally, the ions produced in this region are accelerated upwards by electrodes to a measurement device. A labelled graphic of the resulting apparatus that encompasses these processes can be seen in Fig. 1.4, and photographs can be found in Fig. 1.5. Each of the three sections on the chamber make use of different physics and design principles that together make a flexible and functional ionization machine. Here we tell of the main aspects that we focused on during the design of each section.

The first element of the apparatus is a supersonic beam of oxygen, which is formed in the beam chamber in the left of Fig. 1.4. The reasons for choosing a supersonic beam as a source of molecules are three-fold. First, a supersonic beam contains a region in its center called the zone of silence. In this region, the gas undergoes smooth molecular flow; the molecules interact with each other very rarely [16]. As such, physics done in this region will not be complicated by turbulence or other phenomena caused by clusters of molecules. Second, though these regions are non-interacting, they are much more dense than if we were to simply leak gas into the chamber as a background gas at a pressure that creates a similar rate of interaction

²Usually $10^{-9} - 10^{-11}$ torr

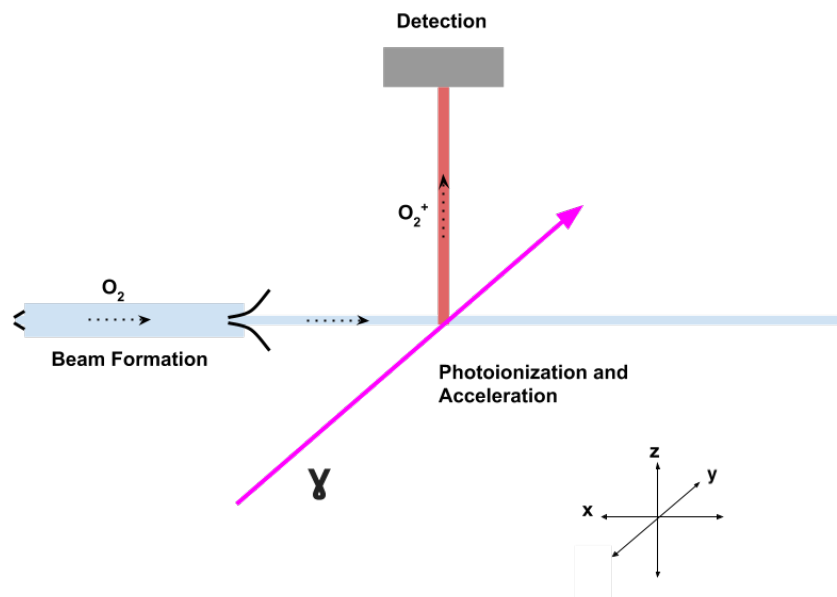


Figure 1.3: Diagram depicting how we produce and measure O_2^+ ions in our test chamber. The oxygen gas begins at room temperature and high pressure in a canister. It is let into the chamber as part of a supersonic beam, where the molecules become cool. The beam then passes through a conical skimmer to reach the ionization region, where it is intersected by the exciting and ionizing laser, making ions. In the same region, the new ions are accelerated towards a microchannel plate (MCP), our measurement device. When they reach the MCP, the quantity of incident ions is detected.

[16]. This density allows us to create a larger number of ions, and thus creates a larger signal to measure than other options. Finally, supersonic beams are cold. Because the gas essentially undergoes an adiabatic free expansion, the internal temperature of the beam is much lower than room temperature (from which the gas originates), without using additional cooling measures [16, 17]. Lowering the temperature of the beam limits the internal states of the neutral oxygen molecules we ionize, which in turn limits the number of states of ion we produce. Using a beam thus partially compensates for the complications of rotational structure. To physically realize a beam, we needed a differentially pumped chamber and an assembly that skims the

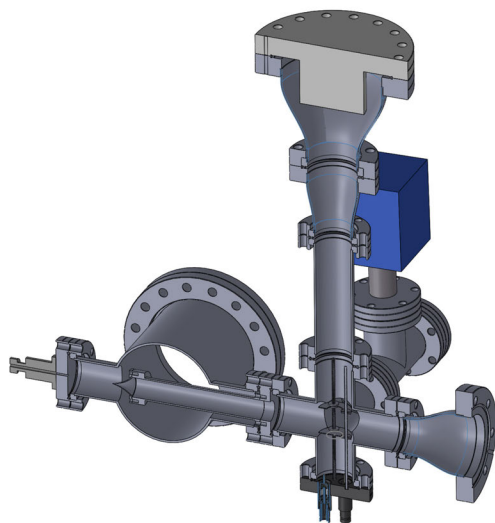
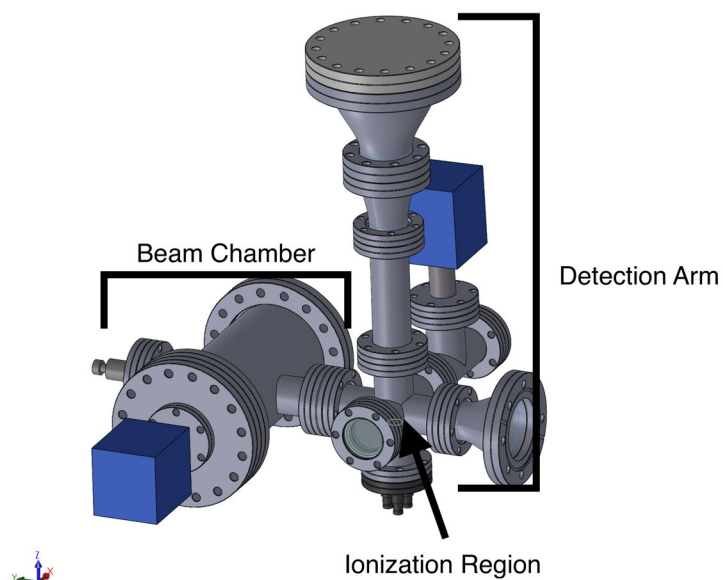
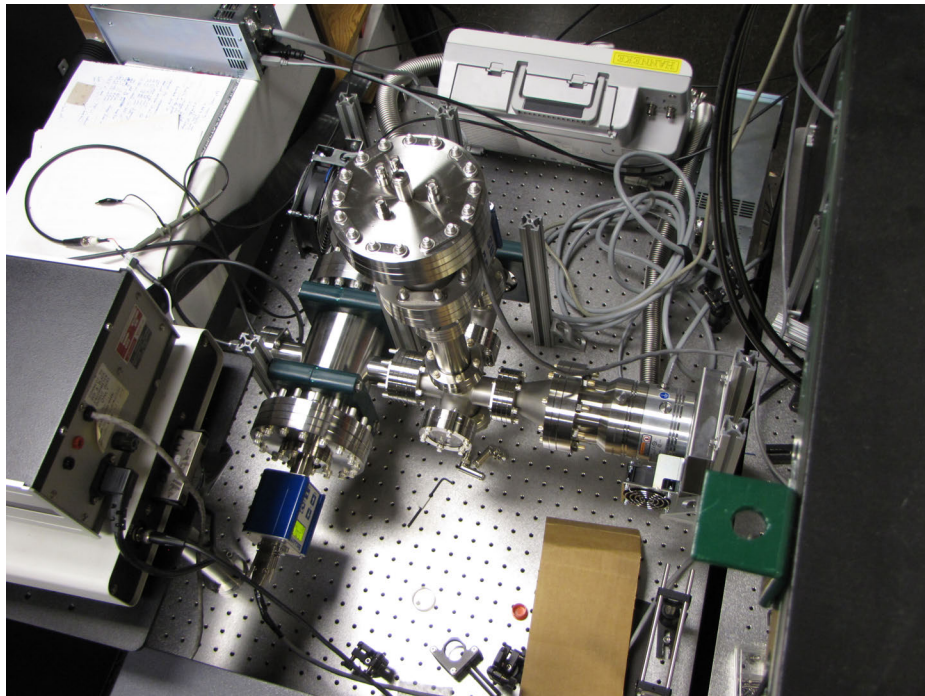
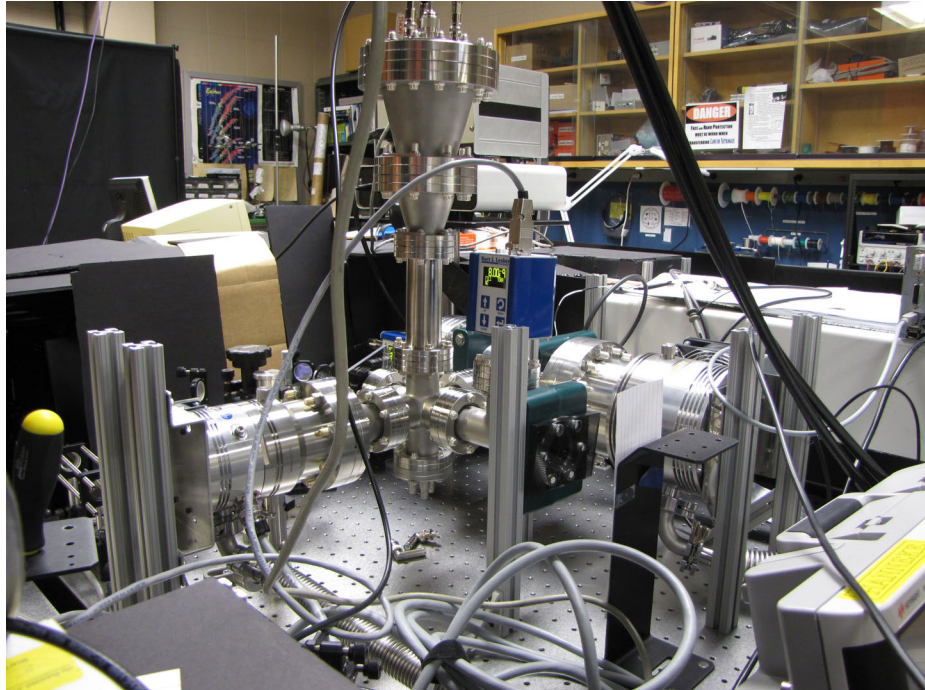


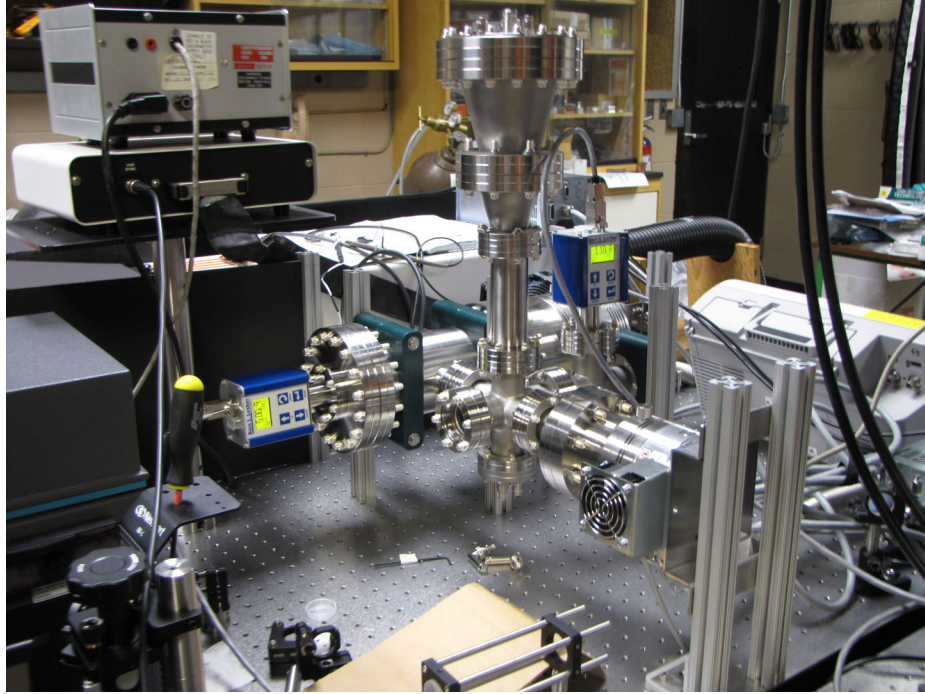
Figure 1.4: CAD files of the test chamber designed to produce ions via (2+1) REMPI and detect total ion yield. On the top, the three main regions are labelled. The beam chamber is where the oxygen enters the chamber in a supersonic expansion, which cools the gas sample. The beam then enters the ionization region, where the laser intersects the gas beam by entering the window visible in the center of this part of the chamber. High-voltage electrodes are also in this area, which accelerate the newly-formed ions up the detection arm to a microchannel plate (MCP), which can measure the number of ions that make contact. The two open-ended flanges are where turbomolecular pumps connect. The bottom image shows the chamber interior with a cut-away, showing the skimmer as a cone in the beam chamber.



(a) View from above



(b) View from one side



(c) View from another side

Figure 1.5: Three photographs showing the completed chamber, one from above and two from different sides. The pulsed valve and beam creation chamber are most easily seen on the left of 1.5a. The ionization region is the central six-way cross in the system, and is visible in the middle of all three photographs. Finally, the ion detection arm is the vertical component of the chamber, and it too can be seen in all three.

warmer edges of the beam to preserve the cool, dense, center for ionization.

The next portion of the apparatus is the photoionization region, seen in the middle of Fig. 1.4, in which the molecular beam is ionized by the laser. Our main concerns for this section centered around maintaining a low background pressure so that the molecular beam, and the ions once created, are not dissipated by background gas. Experimentally, this implies the need for a second vacuum pump to expel gas from this part of the chamber. In addition to the pressure in this part of the chamber, the physical size of this region cannot be so small that the outskirts of the beam reflect off the chamber walls and back into the beam, disrupting more of the molecules/ions[18]. Other than these size and pumping requirements, the main necessities in the chamber design are windows to let the laser light pass into the ionization region.

Finally, we use a simple charged particle detection scheme, seen in the middle to top of Fig. 1.4, to measure the ion yield. When the molecules are ionized in the ionization region between two electrodes at a static high voltage differential, they are accelerated down a tube and onto a microchannel plate detector (MCP). An MCP is an electron-multiplier device that outputs an analog current proportional to the number of charged particles that make contact with small channels on its surface[19]. Of particular interest in this section is the design and placement of the acceleration electrodes, as well as the operating principles of the MCP. The shape and mounting mechanisms of the electrodes can make the difference between focusing the ions onto the MCP or onto the chamber wall. Even if the ions are focused onto the plate, understanding how the MCP produces a signal is necessary to determine the number of ions present in the first place.

Though this is only a glimpse of the factors we encountered during the design and construction of the chamber, it is easy to see that the full apparatus brings together a number of different devices with input from many different areas of physics to get from neutral oxygen molecules to REMPI-produced ions. In-depth discussions about

both the motivating physics and laboratory construction process for each of these sections can be found in Chapter 4.

1.4 Chamber Characterization

After completing the design and construction, we characterized the chamber and initialized the relevant pieces of apparatus to ensure proper function. This starting up process consisted of four main steps.

We first checked if the chamber had any leaks large enough to impact beam creation or photoionization, and if the new vacuum pump worked correctly. To do so, we simply pumped down the whole chamber and observed the rate at which gas was expelled. Within days, the whole chamber was below 5×10^{-8} torr, and after a few weeks of pumping it was below 9×10^{-9} torr. From this, we infer that the pump was working as expected. Though this was probably also sufficient to assert that no consequential leaks were present, we confirmed the chamber seal with a leak-testing device.

After these checks, we moved on to characterizing how the background pressure reacted to gas pulses; both slow pulses to observe evidence of a beam, and faster pulses to mimic the environment that we would work in while trying to photoionize. With the slower pulses, we did indeed find confirmation of beam production in the profile of the pressure change. With the faster pulses, we found that working at 20 Hz pulse frequency was probably not preferable for ionization experiments because of how high the background pressure sits, but that 5 or 10 Hz experiments should work as expected. These pressure characterizations thus provided promising results and helpful input as to the functionality of our chamber. We did discover problems with our pressure measurement system, but they are unlikely to affect the outcome of our experimentation.

Having been satisfied with how the gas behaves in the chamber, we then turned our attention to starting up the MCP. We carefully turned on and monitored the device for any evidence of arcing, which could easily destroy the instrument. Seeing none, we were able to slowly turn up the power supply to the high voltage recommendations without problem. This process also allowed us to monitor dark counts on the MCP, miscellaneous currents detected by the device caused by stray particles or random misfiring. The dark counts were observed to be low in energy and frequency, which signals that data we take using the plate will not be plagued by noisy background.

With the instrumentation working, and chamber operational, the last part of the project we completed dealt with coordination of the gas and laser beams. Since each beam moves at a vastly different speed, and yet they need to temporally overlap to make ions, it was necessary for us to devise a way to be able to change the time delay between the two pulses. The easiest way to control this was to find a way to externally trigger both devices. Though we did not get a chance to really test the program we created on the gas and laser pulses, we confirmed that it produces trigger pulses in the manner we desire.

The process of characterization and starting-up of the chamber is more fully described in Chapter 5.

1.5 Future Plans

Though we have created a molecular beam and a device capable of photoionization and observation, we have not had time to actually measure the ionization yield as a function of frequency. Nevertheless, our current status provides a clear path forward to achieving this initial goal. In the near future, we will begin scanning the parameter space available to us on the apparatus to find ionization signal. After ions are observed, it is only matter of automating a few processes, like frequency scanning and

MCP signal recording, before the REMPI process can be fully verified in our lab.

Once the apparatus has been shown to be able to produce state-selected oxygen ions, we will then transfer some pieces over to our ion-trapping setup to assist in the $\dot{\mu}/\mu$ measurement experiment. In particular, both the molecular beam apparatus and charged particle detection arm will play vital roles in the long-term experiment.

The molecular beam will continue to be used to produce internally low energy states of oxygen. Since the rotational structure makes rovibrational state selectivity through REMPI quite difficult at room temperature, we wish to continue to work with initial samples of cold ions. As such, we will continue to use the beam as a source of molecules. Though some slight modifications may be required when the apparatus is transferred, much of it can stay intact.

Since we also require a way to observe ions in the $\dot{\mu}/\mu$ experiment, our charged particle detection scheme is directly of use. However, some additions will be needed to convert our system to a true time-of-flight device so that we can distinguish between different ions. To distinguish between ionic species, we will likely need to change the length of the arm to improve temporal resolution, and therefore mass resolution. Furthermore, since we will drive the oxygen vibrational transition with trapped molecules, not a beam, some ion focusing devices may be added to work though complications arising from interfacing ion traps with time-of-flight apparatus. In any case, though there will be additions and changes, the electrodes and MCP we designed and characterized in this thesis can also be integrated into the long-term experiment.

While the futures of the beam and TOF device are taken somewhat into account during the sections on their respective construction in Chapter 4, explicit discussion about the short-term plans to observe REMPI, as well as the longer-term plans for implementing these devices on the trap chamber, can be found in Chapter 6.

1.6 A Note

Each of the aforementioned topics requires and deserves more intimate attention and detail. This is done throughout this work, where the numerous aspects of the project are documented and explained more fully. While I enjoyed each conceptual stage of this work for its own reasons, there is one area in which I hope this thesis can be of particular help to future students. Conspicuously missing throughout my time spent on this project was documented guidance on scientific (specifically vacuum) apparatus assembly. While Professor Hanneke and Ryan Carollo were able to provide me with some documented sources, there were many instances in which even those books or websites did not have good direction. In those times, I relied on their personal experience. Though infinitely valuable, such assistance is not available to all, and lack of comprehensive written material on the subject could be daunting to those who wish to embark on such a project, as it was for me. Therefore, while I hope my work and its products assist our lab intellectually and physically for many years, I also want sections of this thesis to serve students in other labs as well. If it is insufficient, as it undoubtedly will be for some needs and desires, I hope that those who find out the answer write it down, and continue to build up an assortment of intelligible and helpful literature on building scientific apparatus. The enjoyment of partaking in science ought not be hindered by lack of knowledge about how to build the device you need.

Chapter 2

Overview and Motivation

As mentioned briefly in the previous chapter, one goal of our long-term experiment is to test the use of molecular transitions as clock references. The added rovibrational degrees of freedom in molecules offer a wider suite of available states to work with than atoms, though this additional structure also makes molecular experiments more complicated. However, the abundance of dipole-forbidden transitions offers a large number of long-lived and narrow-linewidth states [2], [20]. In the long-term project, we will drive a two-photon vibrational transition in oxygen molecules and measure the stability of the transition to test such transitions as clock sources.

The second goal of our experiment is to test the viability of molecules as probes of fundamental physics. Due to properties that atoms do not have, such as strong internal electric fields or large aggregate spin, molecules can provide test environments not possible in large-scale physics due to cost or physical limitations. Molecules are currently being used in experiments on parity violation[21], fifth force searches [22], gravitational sensing [23], and more. In our project, we hope to use the stability of the transition frequency to test the possible time-variation of the proton to electron mass ratio μ [8]. While this value is treated as constant within the Standard Model, many extensions allow or require either monotonic [6] or cyclic time-variation of the ratio [7].

Because the transition we will measure is between vibrational states, whose energy necessarily depends on the relevant masses in the molecule [9], our measurements will be sensitive to variation in μ . Initially, the stability of the vibrational transitions will be used to set a limit on the maximum variation of μ over time, $\dot{\mu}/\mu$. Future versions of the experiment will reach sufficient sensitivity to possibly measure a non-zero $\dot{\mu}/\mu$.

In this chapter, I will discuss in more detail the plans and current progress on this experiment. From there, I will be able to motivate my work within this larger context, and explain how the construction and operation of my photoionization chamber assists us in reaching sufficient molecular quantum control to make these measurements.

2.1 Measurement of $\dot{\mu}/\mu$

At the center of our experiment will be the measurement of the frequency of the transition between the 0th and 11th vibrational states of the oxygen molecular ion. The reasons for working with O_2^+ are relatively simple. Importantly, O_2^+ is homonuclear, and the most prevalent isotope of atomic oxygen has no spin. Because of this, there is no hyperfine structure [10]. This allows us to avoid certain difficulties, such as dark-state population¹, when driving a transition. Being homonuclear also makes intra-electronic state vibrational transitions dipole-forbidden [10], giving the transition the small linewidth essential to both aspects of the experiment. On a pragmatic note, oxygen is also easy to work with because it is well-known. Many of its molecular parameters and characteristics have been extensively documented [11, 12, 24–28], in part because of its ubiquity, making predictions relatively simple compared to less-well characterized molecules.

The particular transition was chosen because of the high sensitivity to changes in μ given available technology [29, 30]. The sensitivity of a state is defined as the

¹Dark state population is when particles enter a state that cannot be excited by the light used in the experiment either due to the wavelength or polarization. As a result, particles that enter dark states are lost from the experiment.

amount the energy of the state changes per a given change in μ . Calculations of the sensitivities of various vibrational states have been previously calculated [8], and a few are tabulated in Table 2.1, along with the energy of the excitation laser required to make the two-photon transition from the ground vibrational state. It is worth noting that the excitation laser for the $v = 0 - 11$ transition is 1063 nm. This wavelength is accessible by a diode laser and fiber amplifier, which can reach tens of watts, making this transition technologically straightforward to drive. Additionally, there are well-known and developed methods for stabilizing these lasers long-term and minimizing the linewidth, allowing us to shrink systematic effects [2, 31–33]. Given cost and time restraints, this transition proves to have the highest μ sensitivity we can access. While higher vibrational states do have higher sensitivity, they are significantly harder to drive. Using the $v = 11$ state, projected uncertainties on the frequency will allow us to measure $\dot{\mu}/\mu$ to less than $6 \times 10^{-14} \text{ yr}^{-1}$, on the same scale as the current best measurement in a molecular system.

Measuring $\dot{\mu}/\mu$ will be a three-step process. First, we will co-trap a large number (~ 50) of O_2^+ and Be^+ ions in our linear Paul trap. Next, we will probe the vibrational transition in the oxygen atoms with an excitation laser. Then, to determine whether or not any O_2^+ made the transition, we will selectively photodissociate ions in the 11th vibrational state to oxygen atoms and atomic ions and measure the masses of particles using a time-of-flight (TOF) device. Existence of $m = 16$ amu particles in the TOF signal will confirm that oxygen ions transitioned to the 11th vibrational state.

Trapping both O_2^+ and Be^+ is important to the experiment for a number of reasons. Notably, because the vibrational excitation is being driven as a two-photon transition, to achieve any large number of transitioning ions, we will need to keep the excitation radiation incident on the O_2^+ for ~ 1 s. Molecular beams often move at hundreds of meters per second, so driving this transition in a beam would require an unrealistic

Table 2.1: Table showing a number of characteristics about some vibrational states in O_2^+ . Specifically, the table includes the wavelength of light required to reach the state from the $v = 0$ state, a measure of the sensitivity of the state to $\dot{\mu}/\mu$, and the wavelength needed to dissociate the molecule in the respective state. Notice that while the $\dot{\mu}/\mu$ sensitivity rises with increasing v , the 11th state has accessible excitation and photodissociation laser wavelengths. Data courtesy of David Hanneke.

v	Excitation λ (nm)	$\frac{-1}{2\pi} \frac{\partial\omega}{\partial(\ln\mu)}$ (THz)	Dissociation λ (nm)
1	10614	28	113
2	5386	54	123
3	3617	80	133
4	2738	104	144
\vdots			
10	1158	231	221
11	1063	249	238
12	984	266	257
\vdots			

scale of physical device. Thus trapping the O_2^+ is absolutely necessary to be able to measure the vibrational transition.

The Be^+ trapping is also vital to the experiment for a number of reasons, despite the ion playing no direct part in the measurement in question. Critically, trapping Be^+ allows us to translationally cool the O_2^+ ions, which then allows us to trap them. While we can and will cool Be^+ ions via Doppler cooling, there is no known cycling transition for O_2^+ , and we thus cannot laser cool those ions. However, by laser cooling Be^+ ions while O_2^+ ions are simultaneously trapped, we will also cool the oxygen ions through a process known as sympathetic cooling. Succinctly, this process works because both species are charged, and so they exchange translational energy through the Coulomb interaction. Laser cooling the beryllium while it exchanges energy with the oxygen will thus remove energy from the oxygen ions, cooling them. Once slowed,

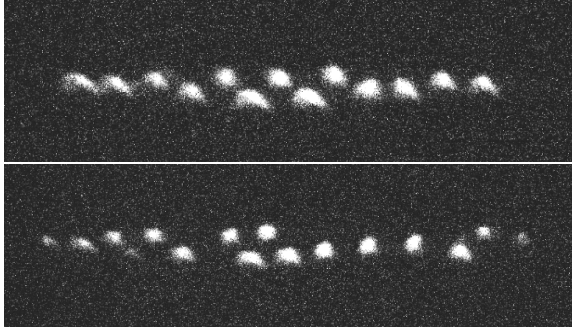


Figure 2.1: Photographs of Be^+ ions in the ion trap. On the top, only Be^+ is present, as is evident by the lack of holes in the image. On the bottom, O_2^+ ions exist in the dark spots, where it appears that bright Be^+ ions should be. The horizontal scale is approximately $250 \mu\text{m}$ long. Figure courtesy of David Hanneke.

the O_2^+ ions will remain in the trap, and can be experimented on.² Therefore, despite the fact that Be^+ are not probed themselves, they are necessary to create conditions that allow us to measure the desired transition.

The Be^+ are also useful because we cannot observe the O_2^+ ions directly. When in the trap, we can see the beryllium ions (on a camera) from the light scattered from laser cooling. Such a measurement is real-time and non-destructive. Lacking a cycling transition, oxygen cannot be observed in this manner. By trapping both species at the same time, symmetry tells us that groups of ions that have “holes” contain charged particles in those holes. To clarify, see the experimental observation of electron-beam ionized oxygen in our trap in Fig. 2.1. The image on the top has bright Be^+ ions without any visible gaps. With the addition of O_2^+ ions in the second image, dark spots exist where bright ions would otherwise be. These are the O_2^+ ions. We can thus use irregularities in the groups of beryllium to determine if we even have oxygen in the trap to experiment on in the first place. We see, therefore, that the trapping of both O_2^+ and Be^+ is instrumental to setting up the remainder of the experiment.

²It is worth noting that internal degrees of freedom cannot be cooled in this process, thus necessitating that the ions we trap have been produced with the correct internal state, namely, the ground vibrational state.

After this cooling and trapping of O_2^+ occurs, we will be set up to drive the vibrational transition and measure its frequency. A schematic showing the transition energy on the ionic potential can be found in Fig. 2.2. To probe and record the energy of this transition, we not only require 1063 nm light, but also a means to measure the frequency to high precision. The former is easily accessible, as mentioned above. We will use a commercially-available extended-cavity diode laser (ECDL) locked to the transition, as these lasers are both economical and precise. The frequency measurement will be more difficult. Wavemeters are a common way to measure laser wavelength in atomic, molecular, and optical physics (AMO) laboratories. These devices take in laser light, and reference it to a well-known transition in a species of gas, often neon. Unfortunately, our current wavemeter will not be able to measure the transition precisely enough to place a low bound on $\dot{\mu}/\mu$ because the linewidth of the transition in the reference gas is larger than the uncertainty in the other areas of our experiment. Instead of using one of these devices, then, we will reference the light to a transition in iodine that is known to much higher precision. This method of referencing to iodine is a well-developed process, and can deliver us the precision we need in the experiment [34, 35]. Higher precision referencing, such as with an optical atomic clock and frequency comb[36], would be able to yield a smaller value of $\dot{\mu}/\mu$, but is expensive and not necessary to first demonstrate viability of technique. A 1064 nm ECDL referenced to an iodine cell will suffice for the current iteration of the experiment to match the best $\dot{\mu}/\mu$ measurements in molecular systems.

Given only these two steps, we would be unable to ever tell when O_2^+ ions transitioned between vibrational states. We require an additional step that state-selectively alters the ions in a way that we are able to determine how many ions transitioned to the upper vibrational state. For this verification step, we will photodissociate the excited O_2^+ ions while in the trap, dump the trap, and measure the masses of the species that were contained via time-of-flight (TOF) spectrometry. If the TOF spec-

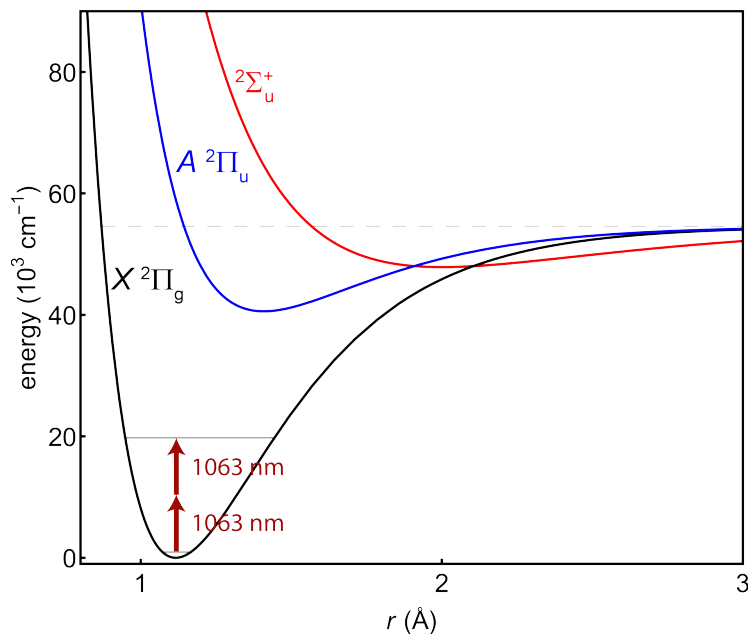


Figure 2.2: Plot of the excitation between the $v = 0$ and $v = 11$ vibrational states in the O_2^+ ion. The black curve shows the ground state potential for the ion, and the blue line an excited state. The red state is the dissociation state. Figure courtesy of David Hanneke.

trometry reveals oxygen atomic ions, we will know that $\nu = 11$ O_2^+ ions had been created.

Photodissociation is a process by which laser light is used to break up a molecule into its component parts. As with photoionization, vibrational splittings are larger than the linewidth of the laser. This means that vibrational-state selective photodissociation is possible. As such, we will dissociate the O_2^+ ions in the 11th vibrational state into $\text{O} + \text{O}^{+3}$. After this occurs, we will have Be^+ , O_2^+ , and O^+ in the trap, but will still only be able to visualize the Be^+ ions. By dumping the trap and accelerating the ions down a time-of-flight (TOF) arm, we will be able to measure the masses of different particles that had been in the trap. Discussed later in more detail, TOF spectrometry allows the differentiation of particles with different mass-to-charge ratios, which O_2^+ and O^+ have. Existence of singly-charged $m = 16 m_p$ particles in the

³See Table 2.1 for the photodissociate wavelengths of various vibrational states

TOF signal will confirm that the laser had been on a transition frequency. Unfortunately, repeat measurements will require reloading the trap each time. Future changes may include an alternate verification scheme, such as quantum logic spectroscopy, to measure the vibrational state of the O_2^+ ions without destroying the sample.

Using this combination of techniques, we will be able to precisely measure $\dot{\mu}/\mu$, either bettering the bound on the quantity and improving the stability of O_2^+ as a molecular clock, or discovering new physics in the form of a time-varying fundamental constant. The odds of the latter, in the initial version of the experiment, are quite small. Later additions, including those I have briefly discussed above, would, over the course of the next few years, bring this experiment to a point where discovery of predicted non-zero values of $\dot{\mu}/\mu$ and competition with clock sensitivity overall limits (not just molecular clock limits) are possible.

2.2 Current Status and Projects

Most progress has been made on the first step of the experimental process; though the other parts are also under development.

We have successfully trapped groups of O_2^+ and Be^+ in our ion trap. A photograph of some trapped ions from our lab can be seen in Fig. 2.1. This trapping is essentially a proof of principle, however; we could not use these ions for the final measurements. One reason for this is that the internal states of the oxygen ions are not well-known, and are likely greatly variable. The unpredictability of internal state comes from the way we obtained these ions through electron-beam ionization, which consists of essentially bombarding energetic electrons into oxygen molecules to strip off a valence electron. The energy of the electron beam cannot be very finely tuned, and, as such, the resulting states of the O_2^+ are not uniform or repeatable. As discussed above, our translational cooling method does not allow us to alter the internal state of the

O_2^+ ions, so we cannot work with ions produced in this manner.

Electron-beam ionization is also currently used to ionize the beryllium, which, though the precision is not as important due to simplified internal structure, still complicates the experiment. The existence of an electron beam at all may lead to the ionization of background gas, which could add undesirable ions to the trap. Additionally, continuous beryllium electron-beam ionization will eventually begin to build up residue inside the chamber, which has a number of undesirable effects including limitation of vacuum level. Thus even our method of producing Be^+ ions is unsustainable.

My work in this thesis primarily focused on the O_2^+ creation problem. Instead of electron beam ionization, we will use photoionization in the experiment to produce the desired vibrational ground state ion. This process relies on laser light, instead of energetic electrons, to excite the molecule to the ionization continuum. The precision is limited by the linewidth of the transition or of the laser; in either case, more precise than the energy of an electron beam. Further explanation of this photoionization process can be found in the following chapter.

By building a device in which we can ionize oxygen molecules and measure the ion yield as a function of laser frequency, we obtained a reference for the ionization laser that will allow us to create O_2^+ ions in the desired initial vibrational state on demand, and allow even some rotational state selectivity. In addition to providing us a valuable reference, such a chamber also served as a grounds to develop the tools we will use to create the O_2^+ ions in the later experiment. Complementing this project, fellow thesis student Christian Pluchar worked on beryllium photoionization, therefore helping us to remove electron beams from the experiment altogether.

The second experimental step is mostly in the design stage. We have not yet purchased a 1064 nm laser for the vibrational excitation, but we have thought a bit about the design of the iodine cell and the frequency referencing mechanism. Nonetheless,

both of these aspects require further work. The photodissociation and TOF measurement steps are also in production, with pieces being produced in Pluchar's and my theses. For the time-of-flight, we have been investigating mechanisms to dump the trap into the TOF arm, and investigating the requirements that the process adds to component design. In my test chamber, we designed a proto-TOF arm to measure the ion yield. For cost effectiveness and convenience, this will be the same arm we use later to measure the remnants of the ion trap following photodissociation, though with some additions. Therefore, its design necessarily took into account what we desired out of it in the later experiment. The creation of the TOF arm is more thoroughly discussed in Chapter 4. The dissociation methods will be covered in Pluchar's work. As seen in Fig. 2.3, the wavelength required for the dissociation of the 11th vibrational state is 238 nm. As it turns out, the beryllium photoionization requires 235 nm. Since the 235 nm laser is more energetic than a 238 nm one, the beryllium photoionization laser Pluchar is working to construct will also suffice to dissociate the excited oxygen. Many pieces of the experiment are thus components of current thesis work.

Succinctly, my work for this thesis has been to create a chamber that can quantify O_2^+ production via photoionization as a function of ionization laser frequency. This chamber makes use of a supersonic oxygen beam to create a cool and dense pocket of ions upon ionization, which are measured by accelerating into a microchannel plate detector (MCP). The ion yield information will allow us to accurately produce ions in known internal states, a vital step necessary for the eventual precise measurement of $\dot{\mu}/\mu$. The theory behind the phototization process we use is well-known and characterized [11–13], so the chamber creation and ion yield measurement are not new discoveries. Nevertheless, this work does help us theoretically by verifying a known process of interest in our lab. This project also moves us materially towards a $\dot{\mu}/\mu$ measurement through our development of pieces of experimental apparatus.

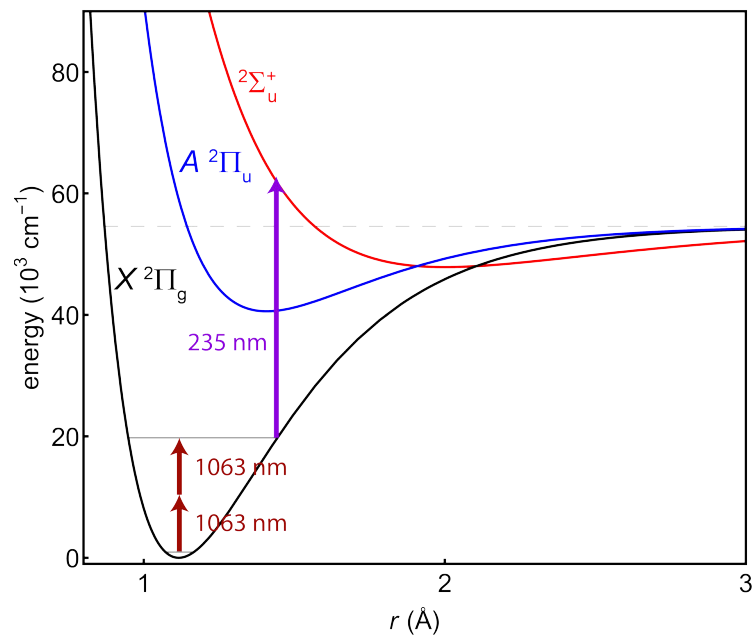


Figure 2.3: Plot showing the photodissociation energy, as the purple arrow, of the $v = 11$ vibrational state in the O_2^+ ion. The black curve is ground state potential of the ion, and the blue line is that of an excited state. The red state is the dissociation state. The dark red arrows signify the vibrational transition discussed in Fig. 2.2. Figure courtesy of David Hanneke.

This work therefore assists in the long-term project both materially and intellectually.

Chapter 3

Photoionization Theory

Before discussing the construction of the components for realizing O_2^+ production in the lab, we must review the intricacies of the (2+1) REMPI process further. Not only are the specificities of the process relevant to the long-term $\dot{\mu}/\mu$ measurement, but they also play a large role in the development of the short-term experimental chamber as well. For the long-term vibrational transition experiment, the O_2^+ photoionization specifics are important because we will need to produce a specific rovibrational state, namely, the ground state. Without knowledge of how the transitions differ from “normal” photonic excitations, we would be grasping at straws if we were to simply pick an ionization laser frequency at random. Additionally, since the process has been documented by predecessors in the field, we have used the REMPI theory to create predictions we can test during the developmental process. For these reasons, though much of the more complex material is relegated to the Appendix for ease of flow, we present here the basics of oxygen (2+1) REMPI theory. It appears from what we discovered in this analysis that we should be able to tune the REMPI laser to produce single-vibration-state and few-rotation-state samples of O_2^+ ions, which will make the $\dot{\mu}/\mu$ measurement possible.

3.1 Overview

At its core, photoionization is a simple process: it is the stripping of an electron from an atom or molecule with light. More precisely, this “stripping” is the excitation of bound electron to the continuum with the energy imparted on the system by a photon. Framed as such, we can apply familiar quantum mechanical methods to understand the system’s allowed angular momentum and energy changes.

There are many forms of this process used in just as many distinct systems. To understand our method of O_2^+ creation, then, we will not focus any longer on general photonization dynamics, but on the specific form we use: resonance-enhanced multiphoton ionization (REMPI). Most generally, REMPI is defined as a multi-stage photoionization reaction consisting of a bound-to-bound transition (a *resonant* absorption) followed by a true photoionization. Though more specific than “photoionization,” there are also many variations on REMPI in different systems. This process is common in molecular diatomics [37, 38]. Even between a given neutral and ionic state, there may be various REMPI processes that link the two. For example, the process that we will use consists of first a 2-photon excitation of the neutral oxygen molecule in the $X^3\Sigma_g^-$ state to the intermediate $d^1\Pi_g$ state followed by a 1-photon ionization to the $X^2\Pi_g$ state of the molecular ion¹. This process is illustrated in Fig. 3.1. If we had funding for or access to other technology (in particular, an extreme-UV (XUV) laser), this same transition could be driven as a 1+1 REMPI process to avoid a two-photon absorption, as has been done before [27, 39].

Nevertheless, because it does not use an (expensive and difficult to operate) XUV

¹The anatomy of the molecular term symbol is similar to those of atoms. The capital Greek letter signals the projection of the orbital angular momentum along the internuclear axis; the progression goes Σ, Π, Δ , etc. The top left number is the spin degeneracy, which equals $2S+1$, where S is the total electronic spin quantum number. The bottom right letter, either g or u , signifies a nuclear symmetry that is only relevant when the nuclei are identical. An excellent description of this symmetry can be found on Herzberg 218 [9]. Finally, there may or may not be an English letter to the left of the term symbol. This signifies an old standard of labelling states. X is the ground state; A,B,C, etc. are excited states with the same spin multiplicity; and, a,b,c, etc. are excited states with different spin multiplicities. For more information see Brown and Carrington 26, 197-203 [10].

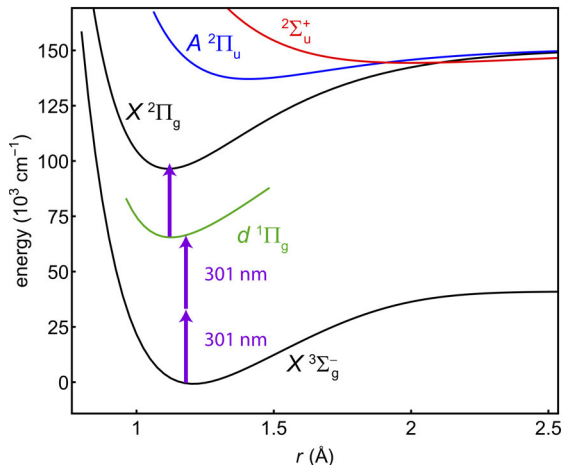


Figure 3.1: Plot illustrating the (2+1) REMPI process between the neutral and ionic ground states of molecular oxygen. The three purple arrows represent the three photons that take part in the process. The lower two are the “2” in REMPI; they drive the two-photon bound-to-bound excitation within the neutral molecule from the $X^3\Sigma_g^-$ to $d^1\Pi_g$ state. These are ≈ 301 nm each. The final photon drives the true photoionization, between the $d^1\Pi_g$ state of the neutral and the $X^2\Pi_g$ state of the ion. The energy between these levels is ≈ 325 nm, but we will attempt to drive it with the more energetic 301nm light as well. Figure courtesy of David Hanneke.

laser system, the (2+1) REMPI between the $X^3\Sigma_g^-$ and $X^2\Pi_g$ states has also been commonly used in experimentation [12, 13]. This popularity is due in part to the relative simplicity of oxygen as a homonuclear diatomic, as well as for its importance in atmospheric science [24]. Despite its popularity, however, understanding the particularities of the process is not trivial. Due to the multiplicity of the ground state, the presence of a two-photon excitation, and the difficulty in describing definite photoionization dynamics, a sample of ions in the ground vibrational state can end up in a large number of ionic states. Being able to understand and recreate oxygen (2+1) $X^2\Pi_g \leftarrow X^3\Sigma_g^-$ REMPI process is necessary to have command enough of the process to guarantee production of molecular ions. Intimate knowledge of this mechanism is vital, especially since rotational state selectivity is desired. By separately explaining the individual components (namely, the excitation and the ionization), a coherent understanding of their combination is made accessible.

3.2 Neutral Excitation

First let us investigate the neutral excitation. In particular, we seek to understand the particular two-photon dipole-forbidden transition:

$$d\ ^1\Pi_g \leftarrow\leftarrow X^3\Sigma_g^-. \quad (3.1)$$

The ground state of oxygen, $X\ ^3\Sigma_g^-$, is a triplet state, as signified by the $S=3$ quantum number which implies a spin of 1. The states are differentiated by values of the total angular momentum $\mathbf{J} = \mathbf{N} + \mathbf{S}$, where \mathbf{N} is the total angular momentum except spin, and \mathbf{S} is the spin. Specifically, the three states are $J = N, N \pm 1$ for a given N state². Thus even were this a single-photon excitation, there would be several options for excited state given a particular N ground state, since a single photon can contribute $\Delta J = \pm 1$. Being a two-photon transition, the options are even more numerous. Though the general $\Delta J = \pm 1$ per photon rule from atomic quantum mechanics remains generally true, there are additional symmetries and propensities that arise from the additional atom in the system.

One type of change we do not have to worry about is that of the vibrational quantum number (which explains why we do not take note of it routinely when referring to the state). The vibrational states of the oxygen molecule are far enough apart (1857 cm^{-1} separates $v = 0$ from $v = 1$ in the $d\ ^1\Pi_g$ state [12]) that tuning the laser correctly will prevent changes in vibrational mode. Given a room temperature or cooler selection of oxygen molecules, the majority will be in the ground vibration state. Since the vibrational splitting is much larger than the rotational splitting ($\sim 10\text{-}80\text{ cm}^{-1}$ [12]), if excited with an energy closer to the transition energy than the splitting (which is easy with a well-tuned laser), we can easily choose a single vibrational state spectroscopically.

²The bolded letters are used to represent vector quantities, while their unbolded counterparts are used to specify a particular value of the quantum number.

The quantum numbers that are allowed to change in well-defined ways are described by the Hund’s cases of the initial and final states³. Only good quantum numbers of both the initial and final state are allowed to change in an ordered manner (e.g. if we have a composite quantum number that is the sum of two others, and the composite is well defined in the initial and final states, it will change in an ordered manner. However, if its two components are not both good quantum numbers of the initial and final states, they may change in different ways). Through in-depth analysis and phenomenological observations, the ground $X^3\Sigma_g^-$ state is known as a Hund’s case (b). The $d^1\Pi_g$ state has been variously characterized as case (b), (d), or (e) [10, 13]. To be safe in our calculations, and for convenience, we look at changes in the quantum number N , which is “good” for both states [13]⁴. Photons, each carrying a single unit of angular momentum, can thus change J by one unit each. In the two-photon excitation, then, J can change by $0, \pm 2$. Given the three possible ground spin states, as dictated by the “3” superscript, we can thus fully describe the possible changes in angular momentum as $\Delta N = 0, \pm 1, \pm 2, \pm 3$.

Since an energy spectrum is more useful experimentally than a set of allowed angular momentum changes, we further seek a description of the energy of the initial and final states. The energies of these states can be calculated by solving the molecular Hamiltonian for a given Hund’s case under certain approximations. For ease we reprint the results here from earlier sources for the energies of the ground state [13]:

$$F_1(N) = B_v N(N+1) + (2N+3)B_v - \lambda - \sqrt{(2N+3)^2 B_v^2 + \lambda^2 - 2\lambda B_v} + \gamma(N+1), \quad (3.2)$$

$$F_2(N) = B_v N(N+1), \quad \text{and} \quad (3.3)$$

$$F_3(N) = B_v N(N+1) - (2N-1)B_v - \lambda - \sqrt{(2N-1)^2 B_v^2 + \lambda^2 - 2\lambda B_v} - \gamma N. \quad (3.4)$$

F here stands for the energy of a spin state, and the subscript describes the energy

³Hund’s cases are approximate characterizations of the angular momentum coupling structure of molecules. See Brown & Carrington 224-233 [10] or Herzberg 218-226 [9]

⁴Since the molecules remain in vibrational ground state, and have low and no spin in two states of interest, N is a good proxy for rotational state in our system. When speaking of “rotational level” we thus are referring to the N quantum number, especially when referring to the excited state.

Table 3.1: Constants used to calculate the energies of both the ground and excited neutral oxygen states. Here we include rotational constants for use in Eqs. 2, 3, 4, and 3.5, as well as the energy splitting between the $F_2(0)$ and $F'(0)$ states used in Eq. 3.6.

	Quantity	Value	Units	Source
$O_2 \ X \ ^3\Sigma_g^-$	B_0	1.4377	cm^{-1}	[13]
	λ	1.984	none	[13]
	γ	-0.0084	none	[13]
$O_2 \ d \ ^1\Pi_g$	B_0	1.68	cm^{-1}	[12]
	D_0	4.34×10^{-6}	cm^{-1}	[12]
$F_2(0) - F'(0)$ Splitting	ν_0	66380.15	cm^{-1}	[12]

ordering of the three spin states. In these equations, B_v is the rotational constant for a given vibration state (i.e. B_0 for the ground vibrational state), and λ, γ are other molecular constants for O_2 . Values for these constants can be found in Table 3.1. For a particular N in the ground state, these equations then give the possible initial energies relative to $F_2(0)$. These equations give us half the information needed for a spectrum, the other being, of course, the energies of the excited states.

As the $d \ ^1\Pi_g$ is a singlet, there is no degeneracy; each N corresponds to a single state. Modeling of this state is not as complicated as the triplet state (think solving a one-dimensional rather than three-dimensional Hamiltonian). In general, the energy as predicted (and verified experimentally by Sur *et al.* [12]) by perturbation theory of a particular N state is given by

$$F'(N') = B'_v N'(N' + 1) - D'_v [N'(N' + 1)]^2, \quad (3.5)$$

where B'_v is the rotational constant, and D'_v is the centrifugal distortion constant, for

a given vibrational state⁵. Values for these constants in the vibrational ground state can be found in Table 3.1. Similarly as above, these energies calculated using this equation are referenced to the $F'(0)$ state.

To get the transition energy between a ground and excited state, we first add on the energy between $F_2(0)$ and $F'(0)$, denoted ν_0 , to a given $F'(N')$. This number is then the energy of the excited state referenced to the lowest ground state, and can be found in Table 3.1. The total transition energy is then given by

$$\nu_{\Delta N,i} = \nu_0 + F'(N') - F_i(N). \quad (3.6)$$

Combining this equation, the allowed ΔN s, and the observation from previous authors that $N > 31$ is rarely observed in room temperature or cooler O_2 , we can now create a list of energies of the allowed excitation routes. It is important to note here also that in the ground state, N can only take odd values due to nuclear spin symmetry [10, 13]. Although we have described all the transitions *allowed* by the perturbative solutions to the molecular Hamiltonians, the routes are by no means guaranteed to be equally likely.

In fact, transitions involving higher values of N tend to be less likely, because higher values of N are less likely to exist in a sample than lower values by standard statistical mechanical predictions. As such, the probability of a transition from N to N' is proportional to the Boltzmann factor of the lower state times a factor taking into account the degeneracy of each state [9, 13]:

$$p(N, N') \approx (N + N' + 1) e^{-F_i(N)/kT}. \quad (3.7)$$

Using the probability as the height and the natural state linewidth (1.7 cm^{-1} [13])

⁵There is no D_v in the earlier energy equations because the earlier authors did not go to as high an order in their expansion

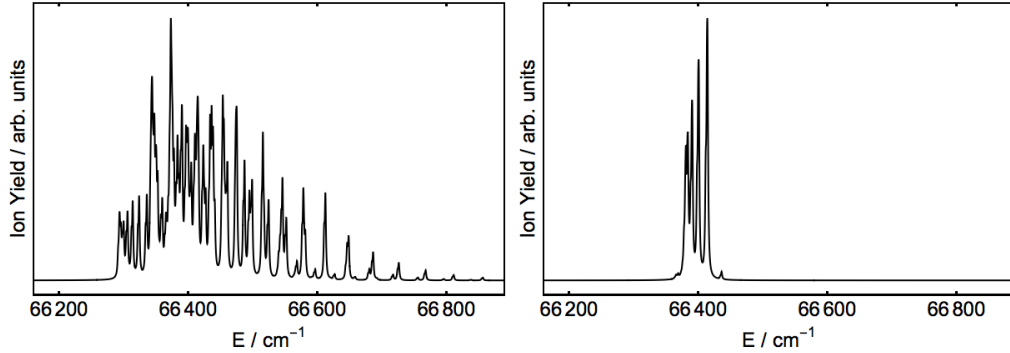


Figure 3.2: Theoretical O_2 excitation spectra at 300K and 5K respectively. Note that there are many overlapping peaks at 300K, while at 5K the plot is relatively sparse. The energy on the x-axis is the two-photon energy needed, so the laser would actually be tuned to half of the values shown.

as the width of a Lorentzian around each frequency, we can use all of this information to predict a spectrum of this excitation at a given temperature. In Fig. 3.2 are plots of the predicted spectra for this excitation with an initial sample of molecules at 300 K and 5 K. The room temperature plot is of interest as it corresponds to ionizing from background gas in the chamber. The 5 K plot better approximates a sample of gas from a supersonic beam, currently a key tenet of our future experimental plans.

Not only are there fewer peaks in the 5 K plot, these peaks consist of lower energy transitions. This suggests that at low temperature, a greater number of excited state molecules created at these frequencies would have a low rotation state than at high temperature. The Fortrat parabolas in [13], which describe the initial and final transition state at each probability peak, confirm this observation. Thus at low temperature not only is the energy structure simpler, but low-rotation-state excited molecule production is also more likely.

Our theoretical understanding is therefore relevant to the overall experiment as it tells us how to improve yield of low-energy excited-state oxygen. Nevertheless, this is only the first step of REMPI. To be able to produce the ions we want, we must also examine how the one-photon ionization process changes energy and angular

momentum.

3.3 Ionization

Just as for the first part of REMPI, we begin our discussion of the one-photon ionization by identifying the particulars of the reaction we want to drive. In terms of molecular term symbols, the ionization is represented as



We cannot apply the same selection rules or propensities to this process as to the excitation, however, because the system fundamentally changes in the process, it is not simply rearranged. When dispersed, the electron not only takes its own orbital and spin angular momentum from the system, but can interact with molecular electromagnetic fields and disperse additional orbital angular momentum as well. These complications make rules difficult to derive, but theorists Xie and Zare [14] have compiled a list of valid angular momentum rules for diatomic photoionization processes. While many of their equations depend on the Hund's coupling cases of the initial and final states, there are some universal rules. Importantly, for any photoionization process, the allowed ΔJ is given by

$$\Delta J = l + 3/2, l + 1/2, \dots, -l - 3/2, \quad (3.9)$$

where l is the orbital angular momentum taken by the departing electron. This rule is easily understood through conservation of angular momentum: the photon has one unit, and the ejected electron has 1/2 unit of spin and l of orbital. Accordingly, different projections of these quantities will create an change of either 3/2 or 1/2 unit. As for the orbital angular momentum, it is, in general, *possible* (but with varying

probability) for the electron to take any integer value from the system. Given only this generic rule, then, we seem to have infinitely many ionic states available from any given intermediate state. Yet this is not observed: rotational state selectivity has been demonstrated in the past for this process in particular [13, 39].

This rule alone thus cannot describe the ionization process. Another factor that plays a role is the conservation of certain symmetries in these reactions. One such symmetry that reduces the set of available ionic states is the nuclear inversion symmetry, discussed in [9]. Normal one-photon molecular excitations can only occur between states with the different initial and final symmetry. Note that the 2-photon excitation will thus change symmetry twice, making the transition between two “g” states possible. Ionization reactions are a different case. Generally, a photoionization can occur between states with any combination of symmetry [14]. That being said, the symmetries of the initial and final states do affect the values of orbital angular momentum the photon can carry: a photon mediating a reaction between two of the same symmetry states must remove an odd l from the system [14]. Thus, while the available states remain infinite, invoking a single symmetry consideration halves the number of available states.

Further limiting either the values for ΔJ or l requires a characterization of the initial and final states with Hund’s coupling cases. The final ionic state is well-known as a case (a). However, the intermediate state has been variously characterized as (b), (d), or even (e) [10, 13, 39] ⁶. Luckily, due to particular electronic state of the excited molecule, the disparities between parity selection rules for different cases fall away, and we’re left with an additional selection rule [14]:

$$J^+ - \frac{1}{2} - N' + l = \text{odd}. \tag{3.10}$$

⁶This being said, we believe the state to be a case (b) state, since the description of the molecule in both theoretical and experimental papers make the most sense with this assumption.

Combining equations 3.9 and 3.10, along with the observation that $N' = J'$ in the excited neutral state, we find that angular momentum is further limited to

$$\Delta J = l - \frac{1}{2} + 2n, \quad (3.11)$$

where n is any integer. Since this limitation on ΔJ still allows for an infinite possible numbers of l , we must resort to examining the probability that different l values are removed, since in fact no strict rule limits the allowed angular momentum changes to a finite set.

As with more routine processes, to find the probability of a particular transition, say from $N' = 3$ to $J^+ = \frac{7}{2}$, one must sum over the squares of the dipole moment matrix elements between all initial and final states that fit the defined transition (over all $M_{J'}$, M_{J^+} , etc). In all, the probability is generally given by, for a Hund's case (b) \rightarrow case (b) ionization [40],

$$P(J, J^+) = \sum_{l=0}^{\infty} \sum_{m_l=-1}^l \sum_{m_s=-s}^s \sum_{M_{J'}=-J'}^{J'} \sum_{M_{J^+}=-J^+}^{J^+} |\langle \eta^+, v^+, N^+ \Lambda^+ S^+ J^+ M_{J^+}^+ | \langle s \ m_s | \langle l \ m_l | \mu | \eta, v, N \Lambda S J M_J \rangle|^2, \quad (3.12)$$

where N , Λ , S , J , M_J have their usual meanings, s , m_s , l , and m_l are the quantum numbers for the photoelectron, v is the vibrational quantum number, and η is a placeholder for all additional quantum numbers needed to specify a particular state.

In theory, given characterization of the molecular parameters and enough computing power, the probability of any particular transition could be numerically calculated. However, a number of factors make this option impossible for us at this time. Particularly, the fact that the final state and initial state are not of the same Hund's case, as well as a lack of expertise on calculational modeling, render these computations too difficult to predict a numerical probability for a given transition. Nevertheless,

reasonable estimates of the likely states can still be generated by analyzing trends of these matrix elements.

While the particulars of how we uncovered these estimates is left to the Appendix, we state the main discovery here. Importantly, we found that in our system, the removed electron removes $l > 3$ negligably often. Using this result to do partial calculations, we find that there ends up being three likely values of ΔJ : $+\frac{1}{2}$, $-\frac{3}{2}$, and $+\frac{5}{2}$. While other changes can technically occur, it seems that these three changes are the only possibilities with non-negligable probability. The first option is most likely, with the latter two having lesser, but approximately equal, probabilities.

The ionic state, being treated as a Hund’s case (a), does not have \mathbf{N} as a good quantum number. As such, the calculations that gave the aforementioned results relied on using the Ω quantum number as “good”. Though ΔJ is limited to three options, each final J state will actually be a component of two seperate Ω states. As such, there are actually six possible distinct ionic states that can be produced from a given excited neutral state.

These six ionic states are not of equal energy (having different J and N values), so better selectivity is in theory possible if the ionization process is mediated by a seperate laser than the excitation step. For more information about single-state selectivity, see the Appendix for future options. Since we do use the same laser to ionize as the excite the molecules, we will produce each of the six options given a particular intermediate state. As such, the spectra in Fig. 3.2 provide essentially all the information we have about the REMPI. These figures dictate the specific intermediary states that the excitation laser produces. Since all likely ionic states that can be produced will be produced, the only real selectivity we have in the process is the choice of intermediate state. As a result, these figures ought to correspond roughly to total ion yield at the excitation frequency. This realization provides us with a relatively simple way to asses our control of the REMPI process in our experimentation: measuring the

total ion yield as a function of frequency ought to produce a spectrum in the form of Fig. 3.2. Additionally, this understanding of the ionization process will be used to choose a specific region of the spectrum to pinpoint during later μ/μ measurements. By choosing a frequency that can access low J' excited neutral states, we can also predispose the gas sample to low- J^+/N^+ ion production.

In particular, we want to create $J^+ = \frac{1}{2}$ ground state ions. Since the excited neutral state is a Π state, and thus has a lowest energy state of $J' = N' = 1$, we cannot create the ions through the most powerful $\Delta J = +\frac{1}{2}$ ionization route. We will thus have to make use of the $\Delta J = -\frac{3}{2}$ band by ionizing out of the $N' = 2$ state in the excited neutral molecule⁷. To get many molecules into this state from the ground state, we must choose an excitation energy that provides a high probability of transition while driving as few other rotational transitions as possible. The highest probability excitation into the $N' = 2$ state from the ground state occurs at 66389.2 cm^{-1} from $N = 1$ in the neutral ground state. Note that while this region in frequency space is densely populated with different rotational transitions in the 300 K plot in Fig. 3.2, it is relatively sparse in the 5 K plot. Thus, our success in using this energy will be dictated by the initial temperature of molecules we achieve. The next most probable transitions into the $N' = 2$ state occur at 66383.5 cm^{-1} and 66374.9 cm^{-1} , from $N = 2$ and 3 respectively. Though significantly less probable than the first transition, these energies lie in sparser (though still populated) regions of the high temperature spectrum. As such, working at these transitions may provide a sample with a higher percentage of ground state ions.

We have thus used theoretical analysis to generate both a short-term prediction that should be easily verifiable with the temporary apparatus, as well as estimates for where we should set the laser energy in the later experiment. Using this understanding of the REMPI process, we are now able to more fully explain the design

⁷See Appendix A to see more on this transition

and construction of the devices we use to actually create the ions and measure the ion-yield spectrum.

Chapter 4

Design and Construction of the Test Chamber

While reviewing and distilling the theoretical knowledge on the oxygen REMPI process is important to complete our understanding of the long-term project, the majority of effort has been placed in realizing this process ourselves. On one level, this realization is important simply to show we can photoionize oxygen with our Nd:YAG laser. However, this process was also used as a developmental ground on which to design the actual pieces of apparatus we will use to create O_2^+ ions for the μ/μ measurement. This second goal forced us to think not only about experimental methods that *would* produce O_2^+ , but methods that will make their production easier and more reliable.

Our final design, seen in Figs. 1.4 and 1.5, consisted of ionization out of a molecular beam followed by acceleration into a measurement arm. How this apparatus fits the experimental aims is best explained by examining the design of subsections of the chamber individually, which we do in this chapter. Specifically, here we explain the benefits, requirements, and design of each of the three major components of the experimental apparatus: the molecular beam, the ionization chamber, and the ion-detection arm.

4.1 The Oxygen Beam

4.1.1 Molecular Beams

A supersonic beam is a decidedly more difficult method to use than simply leaking gas into a chamber. Naturally, then, the reasons for this choice lie not in ease of design, but in ease of experiment. The primary reason for using a supersonic beam is that the gas in the beam is essentially free-expanding into vacuum at a rate faster than the speed of sound in the gas. As a result, there exists a region in the center of the beam called the *zone of silence*, where flow is non-turbulent [16]. Since information about structural impediments; i.e., shocks, cannot travel up the beam due to its speed, the dynamics of the gas are simple, and do not further complicate the ionization process. A second benefit of such beams is their very low internal temperature. Soon after the gas enters vacuum, flow is dense enough for molecules to interact with each other in a manner that cools internal degrees of freedom, resulting in an internally cold beam [16]. If we further select only the center of the beam, where molecules lie with little perpendicular velocity, we can create an externally cool beam in the frame of the molecules as well. In the rest frame, temperature is given by the spread of velocities about the mean. The supersonic expansion naturally produces only a small variance in velocity distribution, creating a low external temperature [16]. Thus using a beam provides us with a dense, cold, and noninteracting set of molecules from which to create molecular ions perfect for experimentation. This is particularly helpful because we have seen that a cold initial set of molecules allows easier production of rotational ground state ions.

Having thus provided the general reasons for using such a beam, it is now important to more intently look at their characteristics to arrive at a method to actually create one. Most generally, supersonic beams of molecules are made by establishing a high pressure differential between the gas source and region of interest. This dif-

ferential is what causes the free-expansion. If the ratio of initial to final pressures is sufficiently high (>2.1), the gas will reach a supersonic speed during the expansion[16]. A diagram of free-jet expansion can be seen in Fig. 4.1. As noted briefly above, we only will use a portion of the beam for our project: the zone of silence. This section is located in the center of the beam radially, between very dense and very turbulent shock regions. Longitudinally, the region sits between the valve where gas enters on one end and a “Mach disk” on the other. A Mach disk is a surface in the beam that signifies the point at which supersonic flow rapidly decelerates and the outer shock waves collapse; after the Mach disk, all gas flow is subsonic [16, 18]. The disk is so named because it is the point where the Mach number, the ratio of the speed of the gas to the speed of sound in gas, changes from greater than to less than one. The zone of silence is thus defined as the supersonic and non-turbulent region of the beam. The approximate position of the Mach disk x_M , and thus a parameter that can affect the construction of a beam experiment, is given by

$$(x_M/d) = 0.67(P_0/P_b)^{1/2}, \quad (4.1)$$

where d is the diameter of the nozzle, P_0 is the stagnant gas pressure before entering the chamber, and P_b is the background pressure in the chamber [16]. Note that larger pressure differentials move the disk farther downstream and thus create a larger region for experimentation. That being said, not all parts of the zone of silence are equally preferable to work with. As mentioned above, a small part of the expansion, even in the zone of silence, takes place with a high gas density. The gas undergoes continuum flow in this region[16]. In other words, the gas flows as a fluid, not as individual particles. Due to the density of the flow, the molecules’ internal degrees of freedom are cooled.

At some distance the density becomes too low for further internal cooling and

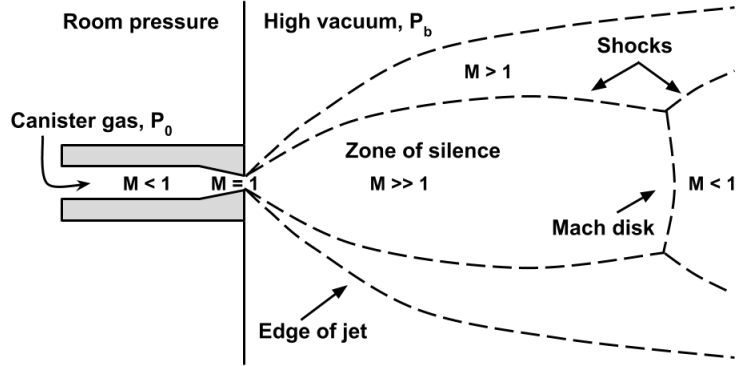


Figure 4.1: Sketch of the basic features of the free jet expansion into vacuum. Of particular note is the zone of silence, the central region of the beam which is highly supersonic (where the ratio of the speed to the speed of sound in the gas, called the Mach number $M \gg 1$) and nonturbulent, so the molecules are unaware of physical obstacles downstream and do not interact with themselves. This feature ends at the Mach disk, where the molecules begin again to flow subsonically ($M < 1$). The outer portions of the beam, between the edge and the zone of silence, are supersonic, but are turbulent, and are hence not ideal for experimentation. Figure inspired by [16]

continuum flow, and the flow becomes molecular. In this region, the gas is well approximated by a group of noninteracting molecules[16]. The separation between these two regimes is called the “quitting surface”. To avoid complications of molecular interaction, and to ensure a relatively constant temperature throughout the beam, we want to experiment in the realm between the quitting surface and the Mach disk¹. The generally desired position x_q of quitting surface with respect to the experimental region can be seen in Fig. 4.2. For diatomics, a good estimation is given in [41] by

$$x_q \approx d \left(\frac{S_\infty}{3.606} \sqrt{\frac{2}{\gamma}} \right)^{\frac{1}{\gamma-1}}, \quad (4.2)$$

where d is the diameter of the nozzle, S_∞ is the terminal speed ratio for the gas, and γ is the heat capacity ratio. In this type of molecule, the terminal speed ratio is

¹The quitting surface is not an actual physical phenomenon, but simply a model that well approximates the point at which interactions are effectively over, so not being past the surface is not essential.

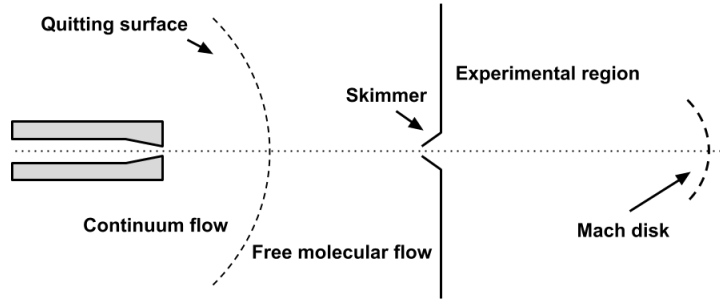


Figure 4.2: Sketch of the ideal relative positions of the quitting surface, skimmer, experimental region, and Mach disk. The quitting surface, where continuum flow ends and particles in the beam cease to interact, should be closest to the gas nozzle so interactions do not affect further processes. The skimmer should be next, so that the center of the beam is captured before the turbulence of the Mach disk. The experimental region is then anywhere after the skimmer and before the Mach disk; the region of cold, noninteracting molecules. Figure inspired by [16]

approximated to within 10% by

$$S_{\infty} = 5.4(P_0 d)^{0.32}, \quad (4.3)$$

where P_0 is the initial gas pressure in torr before entering the chamber, and d is in cm [17]. Discussion of how we got to the relevant parameters can be found in areas of this chapter, but we note here that if the background pressure is 10^{-5} torr the Mach disk is at a distance of over four meters, and the quitting surface is around 18 cm. However, the latter estimate is only valid if the gas is considered to maintain five degrees of freedom. This is almost certainly not accurate, since degrees of freedom are almost certainly not constant in a sample that rapidly cools, but taking this problem into account is quite difficult [17]. Certainly, the quitting surface will be between 18 cm and 2 cm, the estimate for a monatomic gas. Indeed, it will probably tend toward the latter value, since we have observed (in the 5K plot in Fig. 3.2) that we expect very few rotational states to be present.

In general the locations of the Mach disk and quitting surfaces must be balanced against the ability to maintain a certain chamber pressure, and vice versa. As discussed previously, the entering oxygen gas only requires about a factor of two higher pressure than the vacuum background to guarantee supersonic flow. Nevertheless, later pressure requirements for photoionization lead us to desire a background pressure on the order of 10^{-5} torr or lower for the chamber between the valve and skimmer, as per other similar experiments[37]. We keep low pressure by continuously pumping out the chamber. With continuous gas flowing in and out, we reach a steady-state pressure. For a continuous beam of gas, this background pressure P_b is given predictably as

$$P_b = \frac{P_0 C}{Z}, \quad (4.4)$$

where P_0 is the stagnation pressure of the gas before it is released into the chamber, C is the conductance of the nozzle or aperture through which the gas enters, and Z is the pumping speed of the vacuum pump [17]. Even through a 0.5 mm orifice (with a higher conductance than our finite-length valve), maintaining a pressure ratio of $P_0/P = 10^7$ (1500 torr gas canister and 10^{-5} torr background pressure) would require a pumping speed of 230,000 L/s. Such an option is not feasible or readily available. Going to lower differentials, while experimentally more feasible, has its own problems. A minimally supersonic beam with a pressure ratio of 2.1 and similar conductance would lead to a beam with a Mach disk at 0.05 cm.

We avoid making such a choice altogether between easy pumping or distant Mach disk by pulsing the gas into the chamber. By only releasing gas for on the order of one hundred microseconds at a frequency of 10 Hz, we greatly reduce the gas load that the pump needs to expel. In such a scenario, the residual pressure due to a single pulse is now given by

$$P = \frac{P_0 C \delta t}{V} \exp(-t/\tau), \quad (4.5)$$

where P_0 and C are defined as above, δt is the length of the pulse, and τ is a characteristic pumping time for our system given by V/Z [17]. For multiple pulses, the equation remains the same for each individual pulse, such that the pressure due to the n^{th} previous pulse measured directly before a pulse is released, is

$$P_n = \frac{P_0 C \delta t}{V} \exp(-n\Delta t/\tau), \quad (4.6)$$

where Δt is the time between pulses, effectively the inverse of the frequency for low frequencies [17]. After a long time, the total background pressure as measured directly before a pulse is then given by [17] as

$$P_b = \sum P_n = \frac{P_0 C \delta t}{V} \frac{1}{\exp(\Delta t/\tau) - 1}. \quad (4.7)$$

By using these two sets of equations it is usually possible to come up with a set of parameters so the beam will have a large experimental region and manageable gas pumping requirements. Without getting into specific experimental design yet, it is helpful to note that with pulsed beams high pressure ratios are not difficult, and thus neither are conditions for an exceedingly distant Mach disk and a quitting surface near the pulsed nozzle.

Even with these two factors conceptually managed, we still need to avoid unnecessary complications of turbulence and shock by ionizing the radial center of the beam. We do this by inserting a small metal cone into the beam called a skimmer. This device prevents molecules in the outer shock region from making it into the ionization chamber. As well as with any experimental processes (namely, the ionization), the skimmer should be placed between the quitting surface and Mach disk [16], as seen in Fig. 4.2. Luckily, as discussed above, these requirements are often easy to meet. Such a skimmer must also be carefully designed so as not to reflect radially distant high-energy molecules into the low-energy core of the beam, which would lower the

density and uniformity thereof.

Skimming the beam has an additional benefit that we desire: the process naturally selects the “coldest” molecules. While ionizing anywhere after the quiting surface ensures that molecules are frozen in their energy states, the gas is not of uniform energy. The translational temperature of the beam, in general, increases as you move outward from the center, because these molecules have a wider velocity distribution [16]. By inserting the skimmer in the beam, we can select the molecules with the lowest temperature states on average. It also lessens the gas load entering the experimental chamber by allowing for differential pumping.

The ease that a molecular beam brings to the experiment is thus not outweighed by the theoretical requirements of creating such a beam. Though balancing the pumping requirements with a reasonably-sized experimentally viable region is important, pulsing the beam seems to take care of both issues. Additionally, skimming the beam to remove the outer shock provides, without extra effort, the desired low-temperature ensemble.

4.1.2 Realizing a Beam

Given the theoretical requirements discussed above, the basic elements for creating this portion of the experiment are a vacuum pump, a pulsed valve, a skimmer, and an ion gauge to measure the pressure in the chamber. CAD graphics of the beam apparatus, both intact and separated by subassembly, can be seen in Fig. 4.3. How this part of the apparatus fits in the whole test chamber setup can be seen in Figs. 1.4 and 1.5.

For the valve, we chose a Parker Miniature High Speed High Vacuum Dispense solenoid valve, a common choice for many pulsed beam experiments. We chose the 0.02” aperture to minimize the gas entering the chamber, and got the conical nozzle to ensure good beam shape. To physically mount the valve, we drilled a small bore

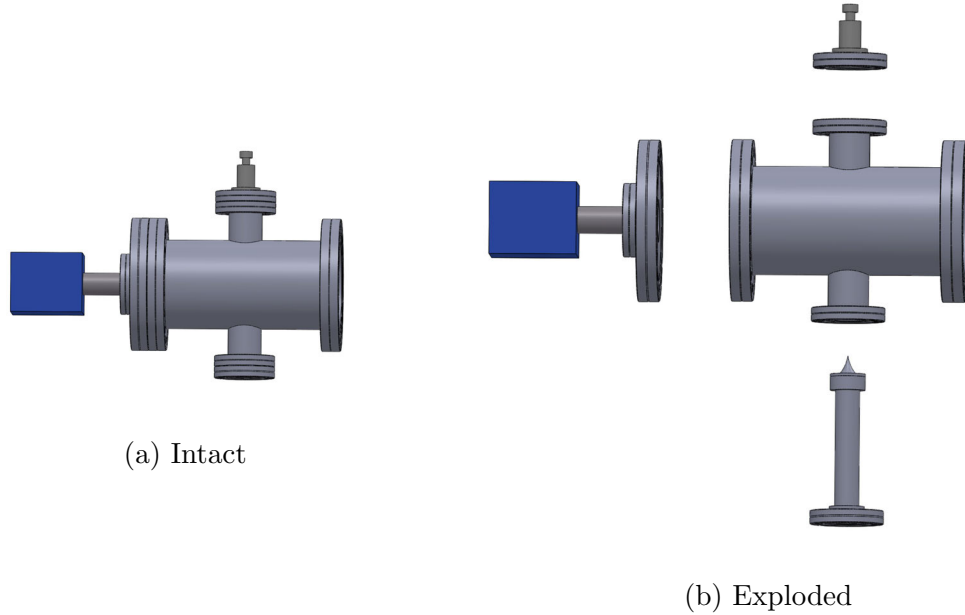


Figure 4.3: Two CAD images showing the design of the beam creation chamber. The image on the left shows how the pieces look when assembled, while the image of the right has all of the components pulled apart for easy viewing. The mounted pulsed valve is seen near the top of both images, and the ion gauge is seen in both on the left. The skimmer and skimmer holding apparatus are not externally visible when the pieces are assembled, and as such can only be seen in the image on the right, near the bottom. Also of note is that the vacuum cross does not have four of the same sized flanges. We use this type of cross so we can attach a larger vacuum pump to the flange on the right, which allows us to achieve a lower background pressure and thus a cooler beam than with a smaller pump.

(0.06”) in a vacuum flange for the gas to get into the chamber and four threaded blind holes to bolt the valve down. The valve also has a groove for a small O-ring which was placed between itself and the flange to create a seal. A photograph of the assembled mount can be seen in Fig. 4.4.

This valve is rated for 2 ms pulses at 28 V, though it is capable of opening significantly more quickly at higher voltages. To get such pulses, we adopted a circuit produced by the Ye group at CU Boulder that raises the voltage of the pulse and its current sourcing ability[42]. It takes in a small pulse (3.3V or 5V digital pulses, e.g.) and a high-voltage source, and outputs a pulse from the high-voltage to ground. Our updated version of the circuit can be seen in Fig. 4.5. We made the circuit mostly

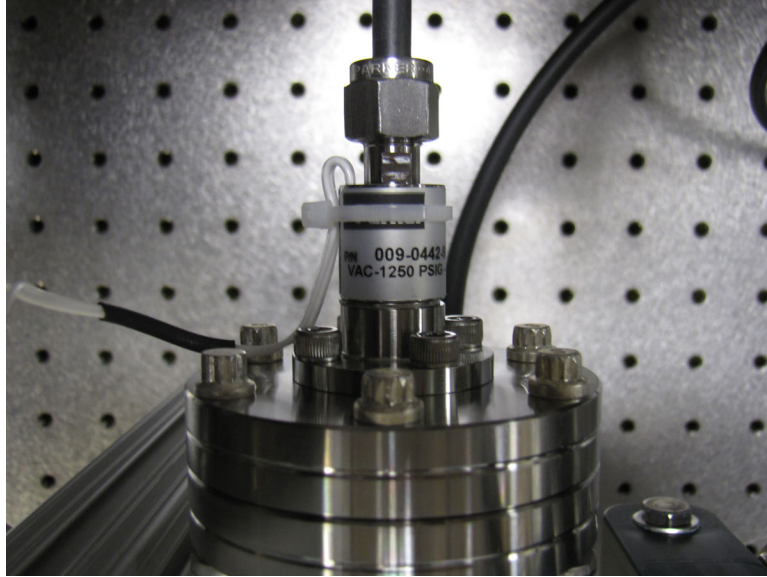


Figure 4.4: Photograph of the pulsed valve mounted on a 2 3/4" CF flange. The incoming gas line (black tubing in the upper-middle) is connected with Swagelok to the valve. The electrical pulsing occurs through the white wire.

only a custom PCB, with high-voltage/low-voltage separation with optical isolators to prevent breakdown. Additionally, the power transistors were kept off the board for better heat sinking. While originally produced for a piezoelectric valve, we found that the output pulses are well-shaped for solenoid valves, as the rise time is short ($<1 \mu\text{s}$). We then tested the circuit and valve together in a small chamber with an ion gauge and our existing vacuum pump (Agilent TwisTorr 84), and found that 400 V (our test supply limit), the valve was able to open for 115 μs or longer. By measuring the voltage across a 1 Ω resistor on the electrical return path out of the valve, we found that the device takes up to 0.4 A at this voltage, showing a 250 W power usage.

Though we had the TwisTorr 84 already, we suspected it was not large enough, with its 64 L/s rated pump speed, to remove the pulse gas quickly enough to maintain a low background pressure. As such, we wanted to use Eqs. 4.5 and 4.7 to predict the pumping speed we would actually need. However, we needed a measure of the valve conductance to use either one.

To find the conductance, we measured how the gas pulses affected the pressure in a temporary chamber and tried to fit this data with either Eq. 4.5 or 4.7. This chamber, a six-way cross connected to a three-way tee (both 2 3/4" CF-flanged), had on it only the pulsed valve, the TwisTorr 84 pump, and an ion gauge. The volume of the setup was approximately 0.5 L.

It turned out that we could not fit Eq. 4.7 to pressure data created by rapid pulsing of N₂ gas². One major reason for this was that the relatively slow sampling rate of the ion gauge prevented us from seeing the true base pressure at high frequencies, since the pressure wouldn't stay low for very long. Not being able to measure the base pressure is an obvious roadblock to using an equation that requires this value.

Luckily, we were able to fit pressure data that was taken by slowly pulsing the valve (1 Hz or less) to Eq. 4.5. We fit data from several pulse lengths: from 115 μ s to 130 μ s in 2.25 μ s increments. One of these fits can be seen overlaying the data from a 120 μ s pulse in Fig. 4.6. By dividing the decay constant from each fit by the source pressure (\approx 1500 torr) and respective pulse length, and finally multiplying by volume, we were able to solve for the conductance C . These trials gave a value of $1.3(4) \times 10^{-4}$ L/s. While not overly precise, the important value for calculating Z is the order of magnitude, so it suffices for our purposes. We repeated these trials with the pump attached to a conical, instead of zero-length, reducer, and found no difference in conductance of the nozzle. This replacement gave the setup a volume of 0.6 L, and thus confirmed for us that a small change in τ did not make a measurable difference in pressure decay.

When we tried to use this value to predict the pumping speed required to maintain a background pressure of 1×10^{-6} torr, we found $Z = 40$ L/s, assuming 20 Hz pulsing of 120 μ s pulses and a 1500 torr stagnation pressure. This value is smaller than the rating of the pump we were using. It turns out that we had forgotten to take

²We used nitrogen because we did not actually need oxygen at this time, since no ionization was occurring.

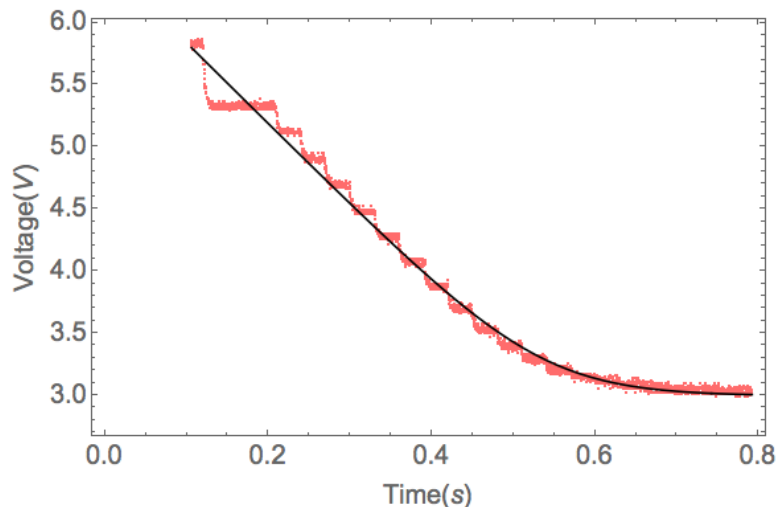


Figure 4.6: Plot of data from a single $120 \mu\text{s}$ pulse fitted to Eq. 4.5. The voltage on the y-axis is related to the pressure by $V = -\log(P) + 10$. The exact values of the fit are not especially enlightening, but it is clear that the data matches a fit of the equation quite well. Fits were done like this for different pulse lengths to measure the conductance of the pulse valve.

the conductance of the tubing between pump and ion gauge into account³. In this temporary setup, the conductance between the beam and the pump was only $\approx 30 \text{ L/s}$, under the necessary 40 L/s to maintain the low pressure we desired. This mishap alerted us to the issue of conductance in the final test chamber. Accordingly, we changed our design to using a reducer cross instead of a uniform cross in the beam chamber, since we could then attach the pump directly to a 6" flange on the chamber, raising the conductance to $\sim 100 \text{ L/s}$, far greater than necessary. The updated design is what is shown in Fig. 4.3. For a second pump, we ended up choosing the Agilent TwisTorr 304, with greater pumping speed than necessary (up to 250 L/s) to ensure the pressure will remain low.

Choice of skimmer was easier than choice of pump, since we had fewer requirements it had to meet. We chose to buy our skimmer rather than make it, as they take extreme precision and engineering to produce. We chose Model 1, with 1 mm aper-

³Nevertheless, the order of magnitude on the valve conductance is probably not far off because the tubing conductance in this dictates the actual pumping rate in the chamber.

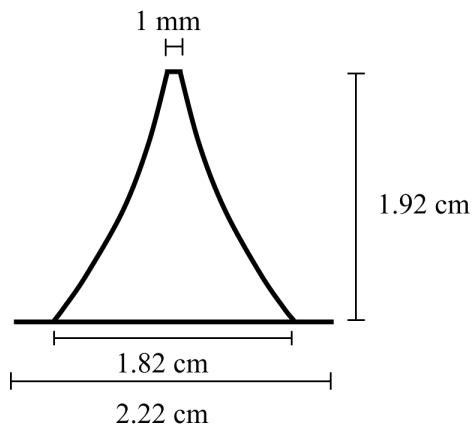


Figure 4.7: Profile sketch of the skimmer with dimensions as quoted by Beam Dynamics Inc. The thickness of the base is rated to be between 50 and 80 μm , while the orifice is 10 μm .

ture, from Beam Dynamics. This company specializes in skimmer production; their skimmers are 10 μm thin at the orifice and precisely shaped to not bounce molecules back into the beam. The full quoted dimensions can be seen in the cross-sectional sketch in Fig. 4.7. We mounted the cone on a machined pipe that held the piece with a ring clamp ~ 5.5 cm from the nozzle. This holder was then fastened to a two-sided flange with a ring clamp. The full skimmer mounting assembly can be seen in Fig. 4.8. Though we initially had wanted a slight groove in the skimmer holder to center the skimmer, the thinness of the metal proved difficult to work with. As such, we aligned the skimmer to the holder by eye. To confirm that this would suffice, we mounted the skimmer assembly into the reducer cross and passed a HeNe beam through the gas aperture, skimmer, and finally through a centering jig on the end of the skimmer mounting assembly. We were able to align the beam to better than 1 mm through the jig, likely signifying a better than 0.3 mm alignment of the skimmer from center. Given that the beam will be much larger than this before it hits the skimmer (else the skimmer wouldn't really be doing anything), we feel this suffices for alignment.

Following this confirmation of alignment, this mount was fastened between the reducing cross and the ionization chamber, such that the molecular beam passed

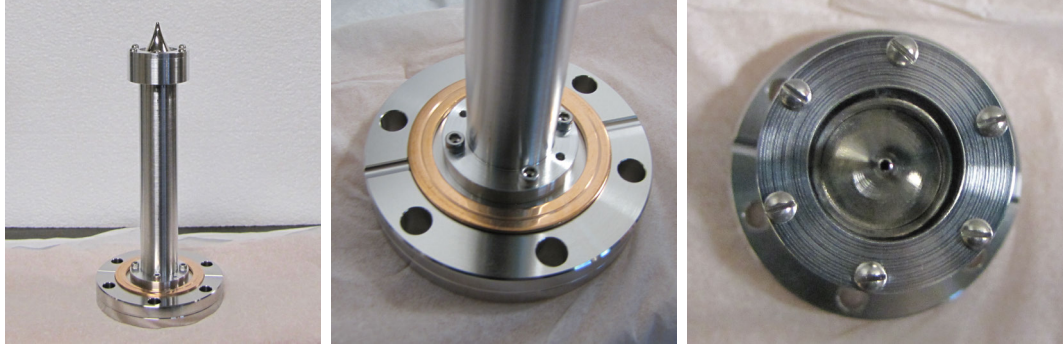


Figure 4.8: Photographs of the skimmer assembly. A side view of the assembly is on the left, with the skimmer at the top, connected via mounting part to a double-sided 2.75" CF flange. The central image is a close-up of the bolt attachment of the mounting piece to the flange. Finally, the right hand image shows the view down the center of the skimmer through the 1 mm skimmer aperture.

from the nozzle, through the skimmer, and into the ionization region. This finalized our design and creation of the apparatus to make a cold, supersonic, oxygen beam.

4.2 The Ionization Chamber

4.2.1 Chamber Design

After passing the skimmer, the molecular beam enters a lower-pressure region with access for the ionization laser and ion detection system. In terms of requirements for chamber design, the simplest and most obvious is that the two beams (molecular and laser) be able to spatially overlap. In addition, the laser must reach a focus very near to the intersection, to maximize the probability of ionization. The (2+1) REMPI we seek to use is difficult to drive, as it includes a 2-photon transition, so maximizing laser intensity is vital. In particular, the intensity of the beam may need to reach as high as $10^{10} - 10^{11}$ W/cm² to achieve good efficiency[15]. For the laser, we use a pulsed Nd:YAG laser through a dye laser using Rhodamine 640/610 dyes, frequency doubled through an LBO crystal to produce pulsed UV light at ~ 0.25 mJ per 10 ns pulse. This suggests we need to focus the beam to 2.5×10^{-6} cm² to adequately

ionize.

Additionally, this chamber must also remain at a low pressure to avoid collisions between background gas molecules and the newly created ions. In effect, this means making the mean free path much longer than the dimensions of the apparatus. A typical pressure to use in photoionization and beam experiments is around 10^{-7} torr [37, 43], which makes the mean free path ≈ 1 km, much longer than any of the setup dimensions. As we could for the beam creation chamber, we can use this pressure, along with other chamber characteristics, to determine the necessary pumping speed for a turbo dedicated to this part of the chamber. If we assume the skimmer is essentially an orifice, the relevant conductance is given by

$$C(\text{L/s}) = 11.6 A, \quad (4.8)$$

where A is the cross-section in cm^2 [44]. Since it has a 1 mm diameter, the conductance is then 0.09 L/s. The volume of this portion of the chamber also includes the measurement arm, and so is between 2 and 3 L. The frequency of molecular beam pulses into this chamber is the same of the pulses of gas into the beam creation chamber, and the source pressure P_0 is $\sim 10^{-5}$ torr (the pressure of the previous chamber). Calculating the necessary Z from Eq. 4.7, we find that the pumping requirements are extremely low, such that it is evident the assumptions used to derive the equation are not valid in the first place. Thus, the 64 L/s pump we have used previously will more than suffice. The pumping will be limited to 30 L/s at the ionization point by the conductance of the tubing, but that speed is still high enough.

While the conductance and pumping are certainly helpful to know, they do not tell us much about the properties of the molecular beam itself in this region. Knowing the speed, temperature, and size of the beam is also helpful for a variety of reasons. The temperature of the beam can be used to better predict final ionic states. The

speed and size of the beam can be helpful to achieve temporal and spatial overlap, respectively, with the ionization laser.

The speed of the beam is simplest to find. Nearly regardless of temperature and density, molecular beams reach a terminal velocity within a few valve diameters from creation [16]. Explicit calculation of this velocity is fairly simple, provided one assume a constant number of degrees of freedom f in the gas during the acceleration phase. Since the quitting surface is much farther than a few mm, this seems reasonable. In this case,

$$V_{\infty} = \sqrt{\frac{2R}{W} \frac{\gamma}{\gamma - 1} T_0}, \quad (4.9)$$

where R is the gas constant, W is the molecular weight in reference to Carbon-12, γ is the heat capacity ratio given by $1 + 2/f$, and T_0 is the initial gas temperature (about 300K here) [16]. This equation then tells us the beam moves around 470 m/s.

Finding the temperature of the beam proves more difficult. In terms of the Mach number M of the beam center, the ratio of final to initial temperature is easily derived from basic thermodynamics as

$$\left(\frac{T}{T_0}\right) = \left(1 + \frac{\gamma - 1}{2} M^2\right)^{-1}, \quad (4.10)$$

where γ is defined as above. However, numerical calculation of the Mach number as a function of distance is not simple. Instead of prediction, the best option is to use equations made by fitting experimental data, as listed in Scoles [16]. Two fitted equations are given, though both provide answers within 1% of each other, so only the more general is reprinted here. Given a distance from the valve x , the Mach number of the beam centerline is given by

$$M = A \left(\frac{x - x_0}{d}\right)^{\gamma-1} - \frac{\frac{1}{2} \frac{\gamma+1}{\gamma-1}}{A \left(\frac{x-x_0}{d}\right)^{\gamma-1}}. \quad (4.11)$$

In this equation, d is the diameter of the skimmer, $x_0/d = 0.4$ is a constant for diatomic room temperature gases, and $A = 3.65$ [16]. Entering $10.88'' \approx 275$ mm for x (consistent with our final design) and 1.4 for γ , we find that $M \approx 34$ at the point of ionization. Plugging back into Eq. 4.10, we see that given these estimates, the beam should be 1.3 K.

Many factors could change this temperature assumption towards higher values, however. Most notably, not skimming the exact center of the beam may have a large effect on the temperature of the molecules. The off-axis Mach number calculations are difficult and require numerical modeling, but it is clear that the above equations describe the center of the beam only. Nevertheless, we predict our temperature to be between 5 and 20 K, a typical range for molecular beam experiments[12, 27, 45].

Finally, to find the radius of the beam in the center of the chamber, we assume the gas undergoes basic Gaussian expansion into vacuum. In this model, the radius of the beam at a given temperature T and time t is given by

$$\sigma(t, T) = \sqrt{\sigma_0^2 + t^2(k_b T/m)}, \quad (4.12)$$

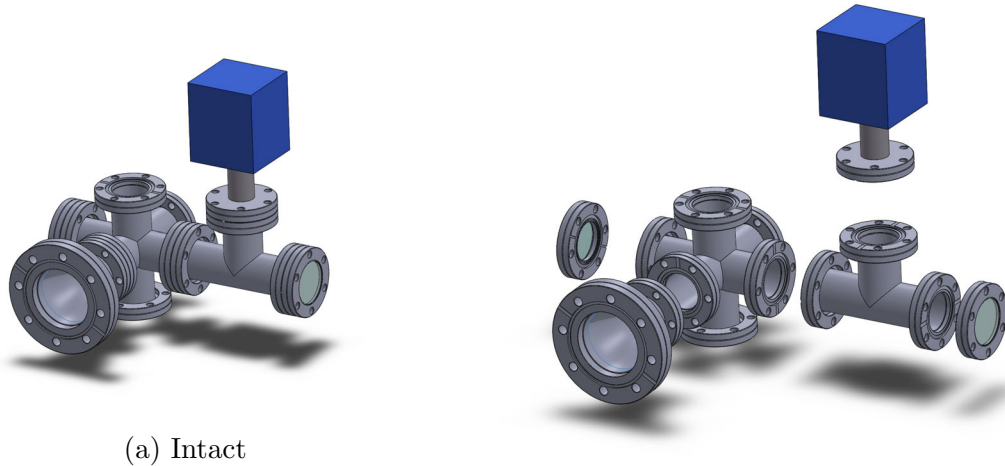
where m is the oxygen mass, σ_0 is the initial beam radius (approximately the radius of the skimmer), and k_b is the Boltzmann constant. We know the mass, skimmer radius, Boltzmann constant, and beam's temperature at this point (approximately 1.3 K). Using the beam speed, we see that the gas will take approximately $\frac{275 \text{ mm}}{470 \text{ m/s}} = 585 \mu\text{s}$ to transverse the distance from the pulse valve. Since the Gaussian expansion assumes the beam begins at the skimmer, we use a time $t = \frac{220 \text{ mm}}{470 \text{ m/s}} \approx 470 \mu\text{s}$ in the radius calculation, being only 220 mm between the skimmer and chamber center. With a speed of 470 m/s and a temperature of 1.3 K, this model predicts a beam radius of 8.6 mm at at this point. Like the prediction of the temperature, this may be somewhat far from reality. Scoles and other authors make clear that Gaussian expansion is

unlikely in all but the least complicated beam experiments. Relatively small tube diameters and short experimental path length may both contribute to the beam size differing from these predictions. Nevertheless, these models give a sense of the scale of temperature and beam size that we will be working with.

4.2.2 The Realized Ionization Chamber

The key physical components for building this part of the apparatus are a six-way cross (to handle the intersection of the laser and molecular beam, and an axis for the time-of-flight measurement), a vacuum pump, laser windows, and another KJLC 354 gauge. We chose a cross of the same size as the skimmer flange (1.5" diameter with 2 3/4" CF flanges) for simplicity. The molecular beam comes through the chamber parallel to the table into a pump on the opposite side of the ionization region. The laser goes along the perpendicular axis which is also parallel to the table, through deep-UV (DUV) fused silica windows. DUV windows are made of especially hard and pure silica to prevent ablation by the laser. Since the time-of-flight equipment takes an entire axis of the cross, we add the ion gauge off a tee attached to the ionization chamber along the laser axis. A mockup of the ionization chamber alone can be seen both as assembled and as its component parts in Fig. 4.9. Its placement in the overall apparatus can be seen in Fig. 1.4 and 1.5.

With the correctly sized Agilent TwisTorr 84 already available in our lab, the pressure concerns were trivial to alleviate. Additionally, the alignment of the molecular beam was taken care of by the alignment of the skimmer, and was thus not a source of worry while assembling this part of the chamber. In fact, the only aspect of the ionization chamber proper (not including the detection apparatus, discussed in the next section) that took much time at all was the alignment of the laser beam through the DUV windows. To do this, we guided the laser beam first through the windows on their own, and then through 3 mm diameter centering jigs. Thus, at



(b) Exploded

Figure 4.9: Two CAD mockups of the ionization chamber. The image on the left shows the pieces as assembled in the final apparatus. The image on the right has pulled the parts apart to better demonstrate what makes up this part of the system. The deep UV laser windows, shown as bluish-gray, indicate the axis that the laser transverses. The molecular beam begins behind the chamber in this orientation. It moves along the axis towards the conical reducer (which holds a vacuum pump) seen in the bottom left of both images. This reducer holds a turbo pump in the final assembly. The final axis, the vertical, is used for the ion detection apparatus.

this time, the laser beam is known to be within 1.5 mm of centered. While this is potentially enough to spatially miss the center of the gas beam if both alignments are off in additive ways, it is likely that the spatial alignment of the two is sufficient. After the beam was centered on both windows, we added a lens rated with a 200 mm focal length on a three-axis translation stage to reach a focus at the center of the chamber. Though the placement of the lens could be off, since we have no way of confirming the beam reaches a focus until we measure ionization, the stage allows adjustments when needed.

The main concern of this chamber was thus the spatial alignment of the pulsed ionization laser. Nevertheless, this was hardly an unusual case of optical alignment, and was fairly simple. Though the alignment and focus of the beam are not known to be perfect, both the angles of the beam and the placement of the lens are easily altered if necessary.

4.3 Ion Detection

4.3.1 Detection Method

The basic requirements of the ion detection arm in our apparatus did not directly use TOF theory. For the test chamber, we just needed a system that could accurately measure an ion yield. The setup we decided on consisted of high voltage electrodes around the ionization region to redirect the new ions, and a microchannel plate (MCP) that the ions would be directed towards, to detect them. Not coincidentally, these are the same basic components of a TOF setup. Though the very basic requirements for the test chamber do not require any further thought, this project provided an opportunity to develop the TOF we wanted on the $\dot{\mu}/\mu$ experiment, so essentially the rest of the theoretical development relied on TOF theory. As such, understanding the basic theory is essential to understand the full design of our ion detection system.

The basic concepts of TOF measurement can be extracted from introductory electromagnetism. The situation is as follows: a particle of mass m and charge q sits in a region between two charged plates with a voltage V between them. It flies along the electric field until it passes one of the electrodes, into a field-free region. Now, with no forces on it, it travels freely down a tube of fixed length l and is detected at the end. Now, we apply the conservation of energy to this scenario, assuming the initial kinetic energy of the particle was small in the direction of applied electric field. We then see that

$$qV = \frac{1}{2}mv^2, \quad (4.13)$$

where v is the final velocity of the particle. Solving for the time the particle takes to reach the detector, we find

$$t = l/v = l\sqrt{\frac{m}{2qV}}. \quad (4.14)$$

In other words, given a fixed V and l , the time a particle takes to transverse the arm is dependent only on its mass to charge ratio. In this ionization experiment, where we only seek to produce and measure a single species of ion, this means that the time between ionization and measurement is *known*, and so aligning a measured voltage with the laser pulses could at least assist in confirming that a signal is due to oxygen, not from stray ions or cosmic particles.

Nevertheless, the full power of TOF is not completely passed by in the test chamber. Molecular beam experiments can often produce molecular clusters, groups of molecules that stick closely together[16]. Since it is a TOF device, our detection scheme will measure single O_2^+ ions at a different time than ion/neutral clusters, since the charge-to-mass ratios will differ⁴. Specifically, the charge of each species would be the same, $+e$, while the mass would differ by at least 32 amu. Solving Eq. 4.14 for the time it would take each species to transverse a tube of length l , we find

⁴It is unlikely that a cluster of ions occurs due to the Coulomb interaction.

that if a cluster and single molecular ion are produced at the same time, they would reach the detector with a time difference

$$\Delta t = l\left(\sqrt{\frac{64m_p}{2e \times V}} - \sqrt{\frac{32m_p}{2e \times V}}\right). \quad (4.15)$$

Typical acceleration voltages for these devices are in the 1 - 5 kV range. With $V = 1$ kV, $\Delta t = l(5.4 \times 10^{-6} \text{ s/m})$, whereas with $V = 5$ kV, $\Delta t = l(2.4 \times 10^{-6} \text{ s/m})$. These times helped determine the actual detector we chose, discussed later in this section. Nonetheless, this is more of a bonus of using the TOF setup in the test chamber. Significantly stricter time resolution limits come from the demands of future use.

As mentioned earlier, we will use our detection scheme as a true TOF device when attempting to measure $\dot{\mu}/\mu$. In this experiment, discussed at length in Chapter 2, we will photodissociate the oxygen molecular ions into a neutral oxygen atom and an oxygen atomic ion, and then measure the existence of the atomic ion by dumping the ion trap. Being able to distinguish between 32 and 64 amu will then be helpful, but really this experiment relies much more heavily on being able to distinguish between 16 and 32 amu; between dissociated atomic ions and molecular ions. Additionally, since we will also be trapping Be^+ at the same time as oxygen, we would like to be able to tell the difference between 9 and 16 amu. There is also a possibility that we create ionic beryllium hydride (BeH^+), and so ideally we could even distinguish between 9 and 10 amu. Using Eq. 4.14 equivalently as in Eq. 4.15, we find that with 1 kV acceleration voltage, the time difference between 9 and 10 amu particles is $\Delta t = l(5.23 \times 10^{-7} \text{ s/m})$, while $\Delta t = l(2.34 \times 10^{-7} \text{ s/m})$ for 5 kV. These times are noticeably shorter than those between molecular and ions and clusters, and thus this difference provides the final limiting factor on the detector resolution. Even though the length of arm may be later altered without much difficulty, the order of magnitude will not be improved by more than ~ 1 . As such, these calculations essentially provide

a limit on ion detector temporal resolution.

There are many options for ion detector. A standard choice for accelerated ion experiments is an electron multiplier device. These devices begin to generate a signal when charged ions are incident on a highly charged plate or channel it has. The impact shakes a number of electrons free for each particle than hits the device, amplifying the signal. These electrons continue to magnify themselves down the device until the signal is measurable when they hit an anode and create a current. Though this amplification is variable since it depends on the number of electrons freed from the initial impact, the resulting signals are generally proportional to the number of incident ions.

Though there are many devices that fall within this range, we chose to use a microchannel plate (MCP). An MCP is a large group (10^4 and up) of electron multiplier channels all cut into a single plate of material[19]. The quantity of multipliers, and their distribution over the surface of a somewhat large area (up to a few square inches) leads to good detection efficiency (up to 85% for 2keV positive ions[19]) even with ion beam spread, an advantage that some other multiplier devices lack. Though not relevant in this experiment, the spatial distribution can also be used to achieve spatial resolution. In addition, optimally configured MCPs still are able to resolve nanosecond scale events, and are thus quite able to meet the time resolution requirements discussed above to distinguish atomic and molecular oxygen, and even for the later experiment between Be^+ and BeH^+ . There are some additional small advantages over other devices, but, in the end, we really chose this type of detector for its ease of use. Due to the good time sensitivity and ability to register ions over a comparatively large surface area, an MCP is simply easier to use than other devices, as it does not require excellent alignment or a meter-long TOF tube in either our REMPI experiments or $\dot{\mu}/\mu$ measurements.

In a minimal case, only accelerating electrodes and an MCP would be required

for us to measure the ion yield in both instances. However, in many experiments, either size of detector or of apparatus make it necessary to implement ion optics to guide the full sample of ions onto the maximally sensitive region of detector. To see if ion optics were necessary for us, we modeled the ion detection arm in SIMION, an eponymous ion simulation software. Using this software, it is possible to alter the voltages of the acceleration plates, distances between the electrodes, and size of vacuum tubes (which are a ground plane) to see if altering existing parameters could provide sufficient focusing effect without additional ion optics. Two of these simulations, one with a centered beam and one with a 3.5 mm miscentering, can be found in Fig. 4.10.

It is easy to see that there are reasonable ways to construct the detection arm on our test chamber without any additional components, though care must be taken not to drive ions into the wall. A sufficiently large voltage on a positive electrode (1-2kV), as well as a slightly negative voltage on the other plate ($\approx -100\text{V}$) was enough to drive the vast majority of the ions to the MCP under a range of construction dimensions. We found that this is the case because we can use the fringing fields between the electrodes and the vacuum pipes to focus the ions. The results of these simulations also were used to get construction dimensions for the apparatus. Specifically, they told us that the electrodes should be ~ 1 in apart for best focusing, and the combination of both electrodes should be kept in the middle of the ionization region, away from chamber walls.

Therefore we see that while we will not necessarily use the full capability of our ion detection method, the future requirements for a TOF arm informed the design of our test chamber significantly. Notably, we found that if an MCP is able to work on the $\dot{\mu}/\mu$ experiment, it will be able to distinguish between single molecular oxygen ions and ion/molecule clusters quite easily, which could help us diagnose problems on the apparatus. Even more importantly, ion simulation software critical to design the

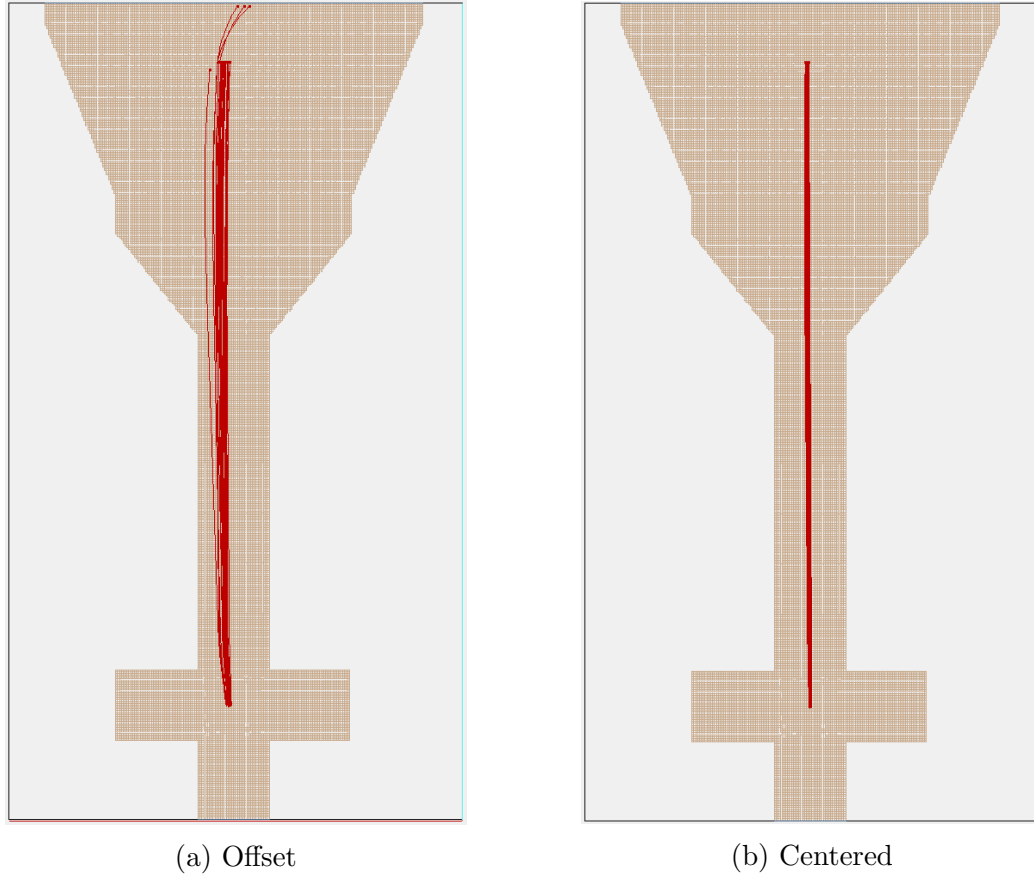


Figure 4.10: Two results from SIMION modelling of our ionization chamber. A 0.5 mm radial distribution of ions begin in the main ionization region, towards the bottom of the images. They are then accelerated upwards towards the MCP by the high-voltage electrodes. In 4.10a, the ionization occurs ~ 3.5 mm off-center. This offset affects the focus and acceleration of the ions, and as a result some do not hit the MCP. However, if the ionization occurs in the center of the chamber, as is the case in 4.10b, all of the ions reach the MCP without problem. No additional ion optics are needed if the conditions in the second image, or in other such conditions, can be sufficiently replicated. Even with minor misalignment, the majority of ions reach the detector. These images assumed a positive push voltage of +1950 V, and a negative pull of -550 V, but +1950 V and -100 V also works, which is the combination we choose. Figures courtesy of Ryan Carollo.

μ/μ experiment was also used to great benefit in modelling the ideal spacing of and potentials on the acceleration electrodes. We thus used the future plans to discover basic design requirements and benefits of the detection arm. In turn, we used these discoveries to inform the construction of the accelerating electrodes, as well as to help select and install the MCP.

4.3.2 Building the Ion Detector

Complications in building the electrodes did not come from the aforementioned minimal requirements, but rather from experimental realities. There were three main obstacles in the construction process. First, we needed a way to transfer electrical signals from the room (and thus the power supplies) to the electrodes in vacuum. Having an electrical connection while maintaining HV-UHV conditions is not trivial; naively just sticking a wire through a hole in the flange would cause a leak no matter how tightly fitting without proper technology. Second, we needed a way to mount the electrodes. Mechanisms of holding the electrodes both are important to think through, for poor choice of mounting could lead to shorting or arcing through the chamber body, which sits at ground. Finally, we also do not want the two electrodes, or their electrical connections, to short through one another. In small-diameter tubing, while trying to maximize the diameter of electrode, it can become difficult to connect both to their respective voltages, while avoiding connection to the walls, without touching both together. All three of these situations are further complicated by the fact that many “normal” lab electrical tools are not UHV compatible. Normal plastic-coated wiring, BNC cables, and Pb/Sn or Sn/Ag/Cu solder are all unusable in low pressures for tendencies to outgas. If these three problems could be solved arbitrarily (i.e. not depending on specific positions or orientations of the assembly) within the limitations of the UHV electronics, then positioning the electrodes as desired from the numerical analysis would not be difficult.

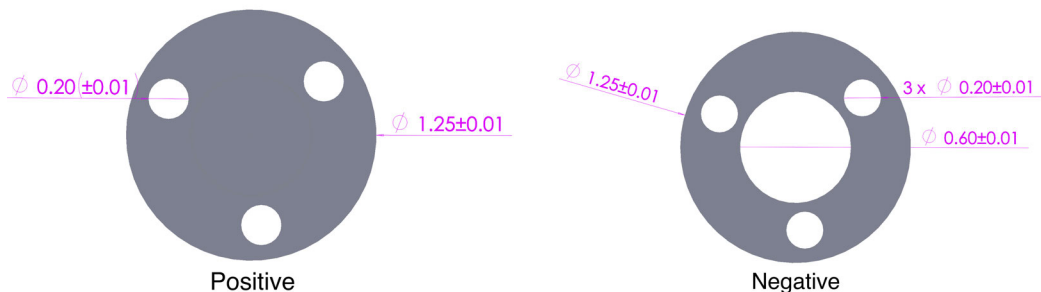


Figure 4.11: CAD drawings of the two electrodes with dimensions in inches. The positive plate is on the left, and the negative plate is on the right, with a bore to let the accelerated ions through. This hole is covered in fine mesh in the assembly, to keep the whole surface area an equipotential. Small alumina spacers fit snugly into the outer three holes of both electrodes, which allows us to mount them on grounded metal rods without fear of breakdown.

Before discussing how we solved these problems with mounting and connecting the electrodes, it is clarifying to describe our basic electrode structure first. The only requirements of the electrode were roundness, flatness, and size (as large as possible within the tube), so the electric field between them was as uniform as possible. Since they still did have to fit in the 1.5" OD vacuum tubing, we were limited to electrodes of this diameter and smaller. In the end, we used stainless 1.25" diameter, 0.025" thick blanks from Kimball Physics as our basic electrode material. The plate that was used for the positive electrode was kept as solid as possible (except for mounting holes), while the negative electrode was bored to allow ions to fly through. The bore was covered in thin stainless mesh, spot-welded to the blank, so as to maintain a uniform potential even where the ions flew through the electrode. The design and dimensions of the two electrodes can be seen in Fig. 4.11. The design of the mounting holes will be discussed as we move through how the aforementioned problems were dealt with, as they were purely functional in design; any mounting system that let the electrodes work would suffice.

The first obstacle was important, but also simply overcome. Though we could not just drill a hole in a flange and stick a wire through it, several companies do

make CF flanges with electrical connections through them. We ended up buying a three-connection SHV flange from MPF, the model A0333-1-CF⁵. MPF uses a tube of ceramic insulator through the flange with a metallic connection in the middle to isolate signal from the ground of the rest of the assembly. These flanges terminate in small pins on the vacuum side. As mentioned, however, we cannot solder wires to these pins. Instead, there are small metal assemblies made specifically for this purpose: they slide firmly over the pin on the electrical flange, and can hold a wire from the desired component in place with a set screw. The metallic body of the assembly forms the connection between flange and component. Thus this problem, while initially appearing difficult, has essentially been solved, as is not an issue with the proper technology.

The second problem, that of mounting the electrodes without coming into contact with a ground plane, is more or less a problem with lack of space in our chamber to mount the electrodes. Were we able to mount the electrodes on a different flange from the electrical connections, there may not have been an issue at all. However, since we were working on a temporary chamber, compactness was always desired. As such, physically mounting the electrodes on the same flange as their electrical connections was the best course of action. It seemed that the easiest way to mount rods onto a flange is to simply screw them on; to bore and thread holes in the flange, and directly mount threaded rods. On the rod, washers and nuts could be used to hold the electrodes in place.

There were then two general options for the material of rod, each with its own problems. Some experiments use ceramic threaded rods. The obvious benefit of these is that the electrodes are, by default, not connected to a ground plane if they're held on the rods. However, being an insulator, these rods can begin to charge up if ions hit the material. This charging can defocus the ions being accelerated and therefore

⁵One connection for each electrode, plus one extra if we need it later. SHV connections since at least one electrode will be biased at several kV.

detract from signal. As such, we sought to minimize the amount of ceramic that could be in the path of the ions. The other option is threaded metal rods. These will not charge up from ion impact because of their physical, and therefore electrical, connection to the chassis ground. However, using metallic support rods also implies that the charged electrodes cannot be in contact with these rods. Taking this into account in our electrode design, the mounting holes (see Fig. 4.11) were machined just large enough to slide ceramic spacers from Kimball in. These spacers were made of alumina, and measured 0.025" tall and 0.126" in diameter with an edge of 0.074" thickness (≈ 1.8 mm). Alumina has a breakdown voltage of over 10 kV/mm, so these spacers were enough to isolate the charged electrode from the grounded rods. To hold the electrodes on the rod, we clamped them in place between two alumina washers (machined away in some areas so as to not be in the ions' path, visible in Fig. 4.13) and stainless steel nuts on each rod. This mechanism also made positioning quite easy, since the height was determined by the position of the lower nut. To get the correct placement of the electrodes, we inserted the assembly into and out of the chamber several times to check and adjust placement of the electrodes near the center of the chamber such that the center of the chamber was free for the laser to go through. We found that not only is this mounting mechanism robust, but also easily adjustable. The final positioning of the electrodes can be seen in Fig. 4.12.

Even though this construction solved the issue of physical mounting, it did not help determine how to electrically connect the flange to electrodes. To get a wire between the electrode and flange, we spot welded the (stainless) wire to the electrode, and connected the other end to the flange as discussed above. For the lower electrode, there were no additional complications: the wire goes nicely from the flange to electrode. However, the wire coming from the upper electrode had to pass between the lower electrode and chamber walls, a space not more than 3 times the diameter of the wire. With an unshielded wire, such conditions are only possible in very high



Figure 4.12: Photograph of the final electrode assembly. A side view of the assembly is shown, in which you can see the mounting washers and bolts holding the electrodes in place. In addition, the bare wire from the bottom electrode, and the Kapton-taped wire from the top electrode, are visible. The major markings on the ruler to the left are in cm.

vacuum (implying a large breakdown voltage), and even then, if the apparatus were bumped, arcing and shorting could easily occur. To get around this, many groups cover electrical wires with ceramic beads. However, these beads did not fit in the allowed space. Instead, we used Kapton tape to insulate the wire. This tape, available from Accu-Glass, has an electrical breakdown of 7500 V. It is also UHV compatible, as it uses a silicone adhesive with an extremely low vapor pressure. By covering the wire by two pieces of the tape, we managed to insulate the wire in a way that fit in the chamber (see Fig. 4.12). This was the last problem with the electrode assembly. After this insulation, we were able to attach the electrode flange to the chamber in the final angular orientation, visible from multiple perspectives in Fig. 4.13.

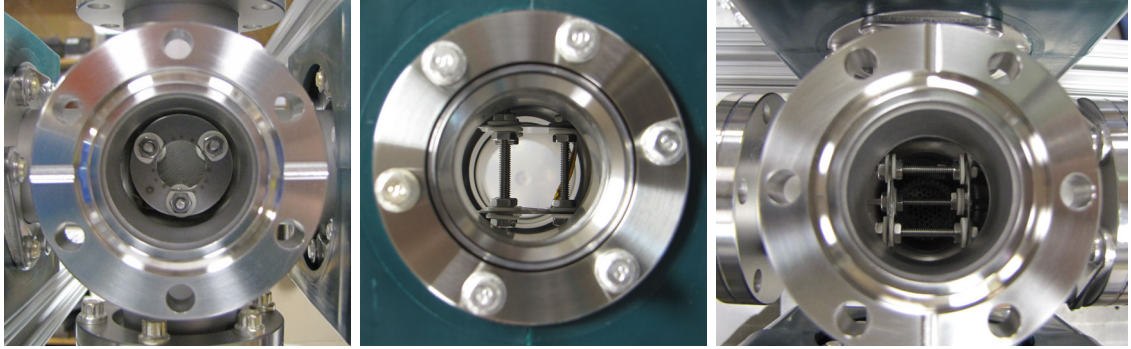


Figure 4.13: Photographs of the electrodes mounted in the chamber. On the left is the assembly from the perspective of the MCP. It is clear from this view that the ground-down alumina washers do not interfere with the ion path (which corresponds to out of the page). In the center in an image of the assembly from the side of the chamber through the viewports the laser will go through, with the negative electrode above the positive. The third rod is behind the rod on the left, so that the laser beam can cleanly pass through the center of the chamber. The right-most image is along the third axis, that of the incident molecular beam, and shows the negative electrode on the left and the positive on the right. Clearly molecules will hit the central rod, but the beam's supersonic nature should prevent that from causing any deviations in beam flow.

The final component in the apparatus is the MCP. While highest control of MCP specifications and responses would be possible by mounting an MCP ourselves, we decided to purchase a full assembly, the C-701, from Jordan TOF. The device can be seen in Fig. 4.15. The assembly contained two MCPs of 18mm active space to record as many incident ions as possible and achieve maximum amplification. They were physically mounted in an optimal chevron configuration, and electrically configured to ensure the best temporal resolution. The anode is also shaped to be impedance-matched to 50 ohms, making connection of the device to scopes and other measurement tools simple. A benefit of buying from Jordan TOF in particular is that, despite the assembly having two MCPs, the company makes their assemblies able to be powered with a single HV supply and a voltage divider. To power the device, then, we used a Ortec 556 0-5 kV NIM power supply and recreated the necessary divider (Fig. 4.14). This combination keeps an approximately 1 kV difference between one

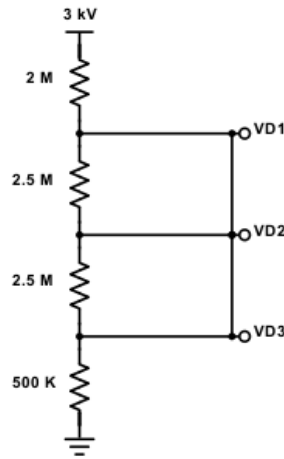


Figure 4.14: Schematic of the voltage divider used to power the MCP assembly with a 3 kV supply. VD1 goes to the first MCP, VD2 goes to the second, and VD3 goes to the anode.

MCP and the other, as well as between the second MCP and the anode. Jordan TOF rates this as a maximum, but since their device powers the plates in this way, it should be operationally safe. The correct powering of the assembly is estimated by Jordan to achieve sub-nanosecond rise times, much faster than we require to confirm our signal contains O_2^+ ions.

We mounted the MCP to a 6" to 4 1/2" conical reducer, which was further connected to a 4 1/2" to 2 3/4" reducer and 2 3/4" straight tube to mount the entire arm to the ionization chamber. The assembled arm can be seen clearly in Figs. 1.4 and 1.5. We pumped down to vacuum immediately after mounting, as extended exposure to air will expose the MCP to enough water vapor that moisture will permeate and ruin the channels. This pumping was maintained overnight before operating the plate to remove as much gas as possible from the channels in the plate. This prevents electrical problems that could arise from having gas present with high voltages from damaging the plate [46].

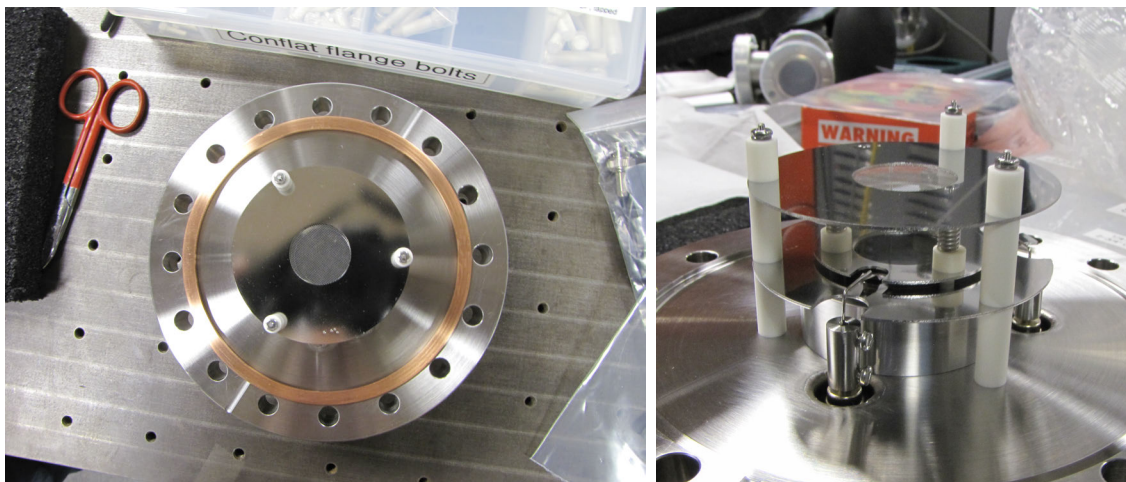


Figure 4.15: Two views of the MCP assembly from Jordan TOF. On the left is a view from directly over the plate, and on the right is a side view that shows the physical and electrical mounting.

4.4 Regroup

In this chapter, we have traced out why and how we designed our experimental apparatus. In the end, our design was influenced by the theoretical physical process we sought to take advantage of in the test chamber, the future plans for certain pieces of apparatus, and specific technical properties of the materials we used. By taking these factors into account, we have assembled a vacuum chamber with which we will first cool oxygen molecules in a supersonic molecular beam, subsequently ionize them with a pulsed dye laser, and finally detect the ion yield from this process with a pseudo-TOF scheme.

Chapter 5

Characterizing the Chamber and Instruments

Simply designing and constructing the experimental chamber of course did not put us immediately in a position to take the ionization spectrum. New devices, however well designed, need to have their functions characterized before experimentation. Aside from this, various pieces of equipment have to be initialized before working correctly, else they will break, or at least not function as desired. As such, despite being a relatively quick process to start up and characterize the apparatus, the process is important to understanding future data. We focus here on characterizing the pumpdown of the chamber, measuring the background pressure during gas pulsing, starting up the MCP, and developing tools to externally trigger the gas and laser pulses.

With the pressure measurements, we confirmed the existence of a molecular beam and made sure that rapid gas pulsing did not lead to too high of a background pressure. By carefully initializing the MCP, we were able to get a sense of the dark count rate and energy, as well. Finally, our work on triggering both beams is directly necessary to achieve photoionization in the near future. Thus each of these startup

procedures contributed to our overall control and understanding of the test chamber.

5.1 Initial Pumpdown

One of the more important characteristics of the chamber for our experimental procedure is the base pressure. While the working pressure may be higher than the true background if we pulse gas into the chamber fast enough, the base pressure sets a firm lower bound. Additionally, too high of a base pressure could signify a leak, which could introduce complications in the molecular beam or ionization processes.

To pump down the chamber, we first had to connect the turbo pumps to backing pumps. Turbos on their own cannot pump down from atmospheric pressure; they're only designed to work with a certain pressure differential across and gas load through them. This means that other pumps are needed to 1) initially pump down the chamber to a low enough pressure for the turbos to work, and 2) remove the gas when the turbo is active to get to a lower vacuum pressure (i.e. backing the turbo, hence the term backing pump). We connected the smaller TwisTorr 84 to an Agilent IDP-3 pump, and the larger TwisTorr304 to an Agilent IDP-7, through their respective gas expulsion ports. Each of these backing pumps was large enough to expel the gas load expected through their respective turbos. They could also pump the chamber down on their own to a pressure of $\sim 10^{-2}$ torr, low enough for the turbos to begin to operate. We use these turbos and backing pumps because they are oil-free, and thus won't contaminate the chamber by backstreaming oil when turned off. The backing pumps are scroll pumps, and the turbos have dry lubrication.

With the pumps set up and the chamber fully assembled, we could begin the pumpdown process. We began by turning on the backing pumps and allowing them to pump out the chamber through the turbos for a few minutes. The backing pumps are loudest when they have the highest gas flow through them, and so an adequate

time to turn on the turbo pumps can be inferred from the relative volume of the backers. When they had quieted, we could turn on the turbo pumps. The skimmer is designed to be able to withstand a 1 atm pressure differential, so there is no concern with not pumping down the two sides simultaneously. Nonetheless, we attempt to do so.

The TwisTorr 84 had been used in previous experiments and was known to be properly functional. We were therefore able to turn on the 84 immediately to accelerate to its normal speed (1350 Hz). However, being the first time using the TwisTorr 304, we used an initial startup sequence to ensure proper function. This process, called a “soft start”, was simply to accelerate the blades of the pump more slowly than a normal startup. Using the “Low Speed” setting on the turbo controller, we accelerated the blades to a lower speed than for their normal operation, to make sure it ran smoothly. When the pump accelerated properly, and worked for a few minutes at this speed, we turned the speed up to the full 1010 Hz frequency.

Between the initial starting of the pumps and the acceleration of the new pump to full speed, we turned on the ion gauges in the chamber to measure the pressure. This allowed us to monitor the pressure both before and after the skimmer (see Figs. 1.4 and 1.5 to see the placement of the gauges) over time. We measured the pressures in each of the chambers frequently over the first hour to see how fast the chamber pumped down to near base pressure. This data can be seen in Fig. 5.1. Though the plot should be a negative exponential (linear on the log scale), we see that the pumping actually goes through two exponential processes. We attribute this to it being the first pumping down of the chamber: many components had gas absorbed in them, and the outgassing into the chamber caused the pressure to stay higher than expected in a clean chamber. The first, faster rate of pumping seen in the first five minutes likely removes most of the background gas in the chamber. The next, slower

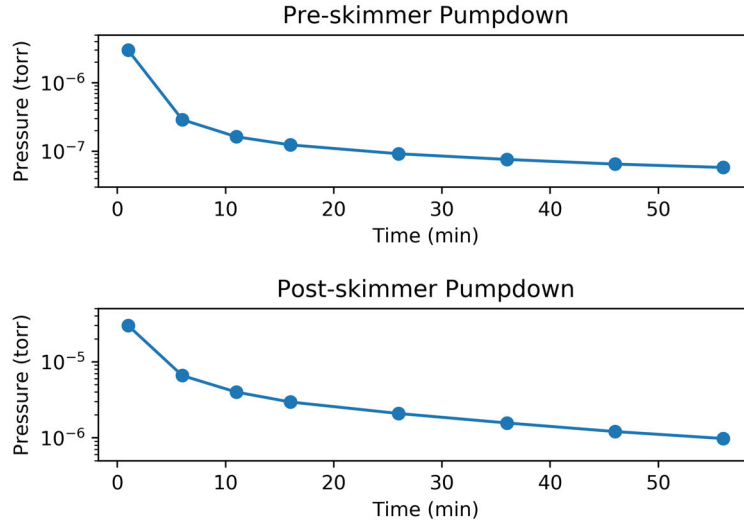


Figure 5.1: Plots of the pressure dropping during the first hour of the pumpdown of the new chamber. Though the pre-skimmer chamber pumps down faster (thanks to a larger pump), the rate of pumping appears similar in each chamber. Furthermore, this rate is not a simple exponential curve (they would appear linear). Instead, the log plots appear to be sums of two lines, signifying a faster pumpdown rate of free gas, followed by a slower pumping of trapped gas and virtual leaks. Though these plots only chart the pressure for an hour, the chambers eventually reached base pressures in the range of 10^{-9} torr.

decrease in pressure is likely due to virtual leaks and outgassing of components¹. This outgassing only lasted a few days. After that long of a time, we reached a relatively steady state around 8×10^{-9} torr before the skimmer, and 1.1×10^{-8} torr after the skimmer. These numbers dropped slightly over the course of the following weeks, but less than an order of magnitude each, signifying a bottoming out of the pressure.

Getting to this high of vacuum signifies that we had no major leaks in the chamber. We confirmed this also by leak-testing the device with a Pfeiffer Helium Leak Test station, on both sides of the skimmer. Given that the chamber was now known to be securely assembled and was able to reach lower vacuum than we needed for the beam (recall a goal of $10^{-5} - 10^{-6}$ torr for the pre-skimmer background pressure while

¹The MCP is an especially egregious culprit in outgassing. Although it was exposed to air for less than a half hour, the microchannels on the device absorb lots of gas very easily. As such, it can take a while to fully remove the gas in vacuum.

operating), we were now ready to test out pulsing gas into the chamber. This would allow us to see if gas was making it past the skimmer (hopefully in a beam) and also give us an estimate of the background pressure we could expect while constantly pulsing the gas, two pieces of information necessary to improve our predictions and understanding of the beam we would create.

5.2 First Gas Pulses

Confirming the existence of a beam and measuring the background pressure during pulsing are done with the same process: pulsing gas into the chamber and looking at the pressure changes on the ion gauges. However, the two are demonstrated most clearly using different pulse frequencies. Just showing the existence of a beam is better shown through slow pulses, such that a pressure rise and exponential decay can be seen in the post-skimmer chamber. Since these are not the conditions that we will use when experimenting (ideally 20 Hz), data from such runs cannot be used to approximate the background pressure under experimental conditions. To get a grasp of that, it is better to pulse the gas at possible running frequencies.

Each of these conditions were fairly easy to create and measure. By pulsing N_2 through the valve at 1 Hz, we were able to clearly see pressure spikes on the post-skimmer ion gauge. The gauge did not simply record a slow increase as may be expected from a general increase in pressure before the skimmer leaking into the other section, but instead showed a quick increase and exponential decay of pressure synchronized, and slightly delayed, from the pressure spike in the pre-skimmer section. This data can be seen in Fig. 5.2. While we cannot be sure of the size or shape of the beam in the later chamber with this information, it seems reasonable to assert that this observation confirms that some type of beam is present. The characteristics of the pressure increase we see do not agree with gradual leaking of gas between

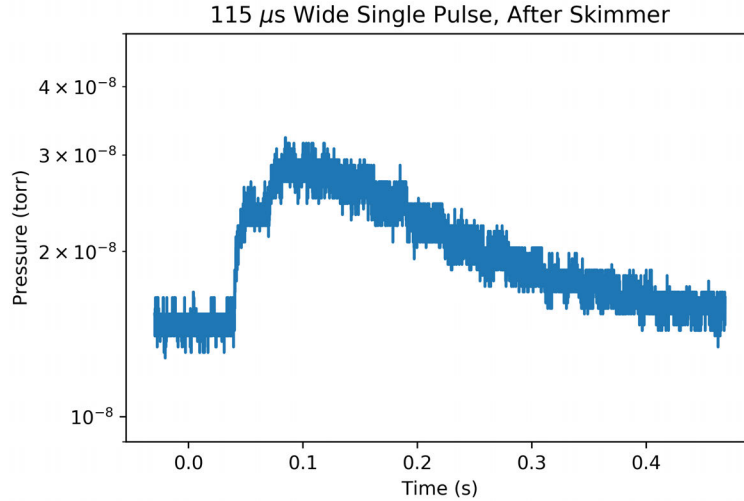


Figure 5.2: Plot of the pressure as measured after the skimmer from a single gas pulse. The exponential shape of the pulse implies a quick rush of gas past the skimmer, likely representing a beam rather than background gas leaking in from the pre-skimmer chamber.

chambers.

This confirmation of a beam allowed us to then speed up the frequency of the pulses and estimate how fast we could expect to add gas to the chamber while maintaining conditions suitable for our experimentation. In Fig. 5.3, we see the pressure measured when pulsing the gas at 5, 10, and 20 Hz. There are a few notable features of these plots.

Most relevantly to why we took this data, we find that the background pressure in the pulse chamber remains around 10^{-5} torr in at least the 5 and 10 Hz plots. Predictions of the base pressure using Eq. 4.7 would indicate that ideal conditions would have background pressure at 10^{-5} torr or lower, which we are able to achieve. Unfortunately, it is not clear, due to the temporal resolution of the gauges, that the 20 Hz run maintains a similar pressure.

These observations come with a caveat, which also happens to be the root of the second item of note we understood from these plots. In short, the gauges are not entirely trustworthy. This was somewhat demonstrated when measuring the conduc-

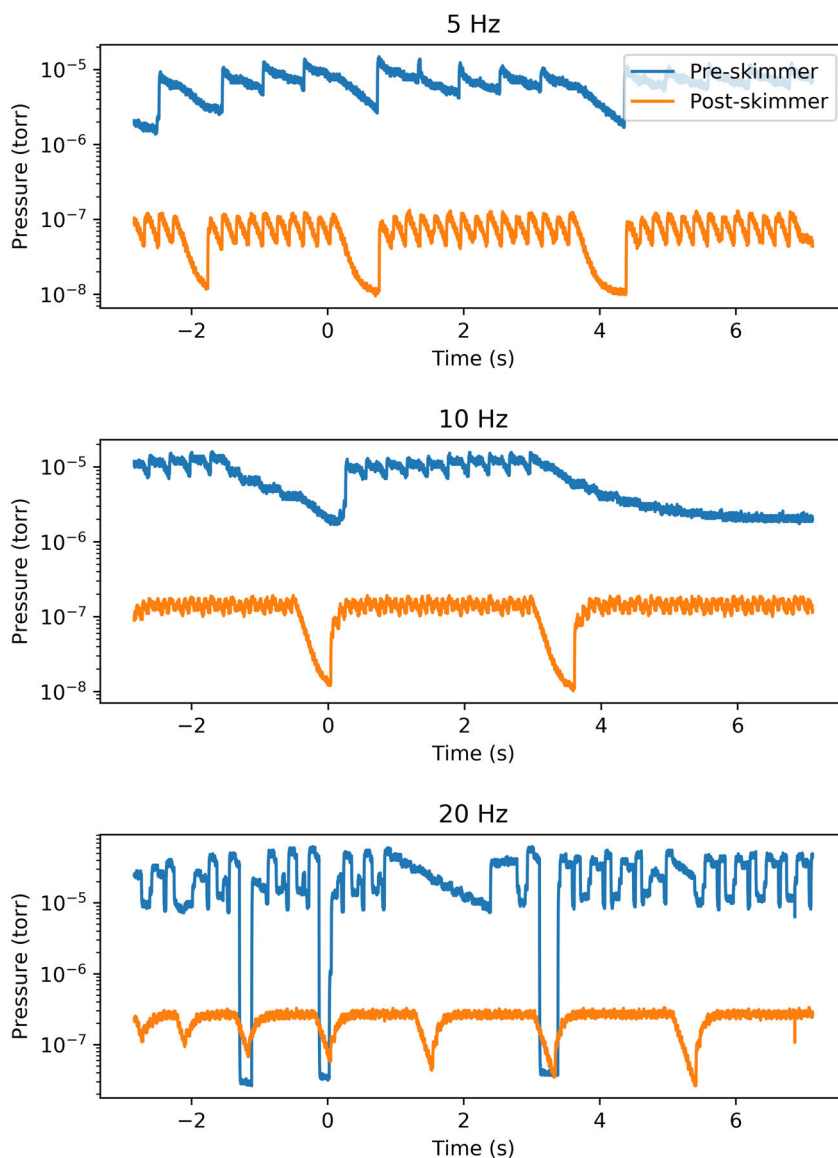


Figure 5.3: Three plots of the pressure before and after the skimmer during different frequency gas pulsing. The plots display several prolonged pressure drops, which are when we stopped sending pulses. Other irregularity, especially that seen in the higher frequency plot, is due to ion gauge controller malfunction. In terms of operating frequency, we see that on the post-skimmer side, the base pressure remains below 2×10^{-6} torr at even 20 Hz. From this perspective, physics in the chamber can work at any frequency sampled here. However, on the pre-skimmer side, the base pressure gets quite high while operating at 20 Hz. At 10 Hz, though, it hovers around 10^{-5} torr, which should be able to produce a cold beam. Thus, these tests show us that we will want to work below 20 Hz.

tance of the nozzle (see previous chapter), but became strikingly apparent when taking this data. As you can in Fig. 5.4, the electronics on the gauge in the pre-skimmer chamber seem to miss some pulses that still appear in spikes in the post-skimmer pressure, even at low frequency. The figure also makes clear that the electronics of both gauges exhibit this behavior, because we switched the electronics and saw the same phenomenon. However, when we did this switch, the controllers reacted differently to missing a pulse. One controller continued a slow linear voltage decay from a previous pulse when it missed a later one, as seen in the top plot in Fig. 5.4. In contrast, the other controlled showed a normal decay of the previous pulse before it missed one, seen in the lower plot. This difference in response quality/resolution we think can be explained by worse calibration of one gauge controller than the other. Whether we did something to cause this discrepancy or if the factory settings differed has yet to be investigated, but we are fairly confident that the difference in resolution is not “real,” but rather induced by discrepancies in the ion gauge controllers themselves.

However, the original problem of the missing of pulses on the high-pressure side remains completely anomalous. We suspect this problem may be related to the fact that the emission current used to actually measure the pressure automatically changes in the range between the base pressures and the peak pressures when we observe the apparent misfiring. This explanation is bolstered by the fact that the problem appears to depend on the amount of gas added to the chamber. By scanning the pulse width from 100 to 130 μs , we found that the “bad” controller recorded the first few pulses correctly, but began to act anomalously as they got longer. This phenomenon can be seen in Fig. 5.5. Despite these issues with gauge controller operation, we believe that the background pressure readings remain valid, though especially at higher frequencies we may only trust the order of magnitude.

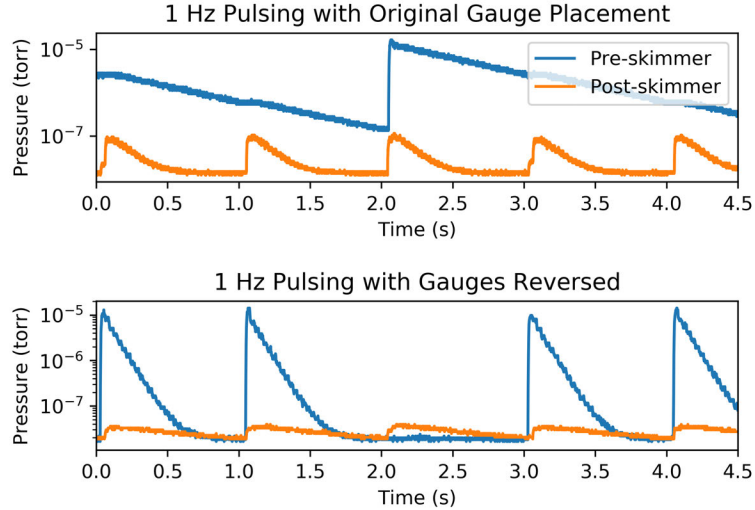


Figure 5.4: Two graphs showing the change in pressure both before and after the skimmer caused by 1 Hz pulsing of $120 \mu\text{s}$ long gas pulses. In the second plot, the ion gauge electronics were switched. Notably, the gauge used initially after the skimmer, and before the skimmer in the second plot, displays higher resolution and better response than the other gauge, regardless of position on the chamber. However, both gauges “miss” some pulses when on the pre-skimmer side, for reasons we do not know.

5.3 Starting Up the MCP

Besides measuring and understanding the basic gas dynamics, we also had to initialize and characterize the MCP. Testing that the MCP is operational before use is recommended to avoid arcing, as well as to get a measure of the “dark counts” of the detector.

Arcing is a concern because the small size and large number of channels in the plate usually hold gas for a while in the device. If the voltage across the plate gets too high with gas present, breakdown of this gas can occur and seriously damage the whole MCP. As such, the first powering up of an MCP should be done by slowly increasing the voltage while monitoring the signal out. Arcing would appear as noise on the output channel.

The dark counts we seek to characterize are not due to true dark current in the device, but rather are usually due to firing of the electron multiplier process by

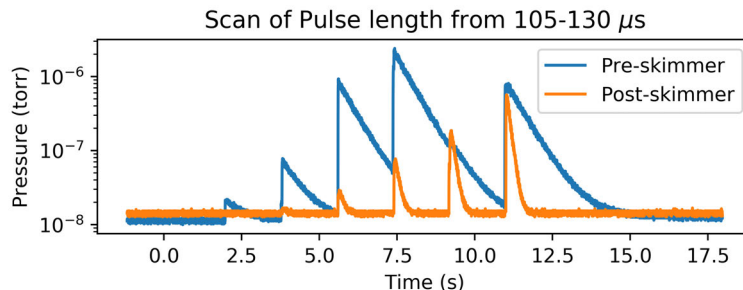


Figure 5.5: Plot of the pressure changes before and after the skimmer due to a chain of increasingly long gas pulses, from $105\text{-}130\ \mu\text{s}$ in increments of $5\ \mu\text{s}$. While the pre-skimmer data appears to be consistent with the post-skimmer data for the first few pulses, the pre-skimmer gauge completely misses the 5th pulse ($125\ \mu\text{s}$), and likely does not measure the full pressure for the last, and longest, pulse. This data supports the idea that the gauge aliasing is due to large changes in pressure in some way.

miscellaneous (often cosmic) particles. These counts will be present even when taking data, so getting an idea of average size or energy is necessary to getting a good grasp of uncertainty in measurements.

Once we had the power supply, voltage divider, and MCP electrically connected (see Chapter 4 for details), we linked the signal output of the MCP to an Ortec VT120C Fast Amplifier, and then to an oscilloscope to real-time monitor the signal.² We then slowly turned up the voltage on the supply, watching the output. Even going up by 100V at a time to the full 3 kV input, we saw no evidence of arcing, likely thanks to the fact that we had pumped down on the MCP for over a week, so any residual gas should have been gone.

We did manage to see dark counts from the MCP. They were relatively infrequent ($\sim 10/\text{s}$), and so at least qualitatively should not interfere much with an actual signal from a sample of ions from the beam. A simple histogram counting the distribution of maximum heights of 50 dark pulses can be found in Fig. 5.6. While this is helpful in telling us that the pulses do follow a distribution, the better measure is of the

²We used an amplifier to see possible arcing or dark counts earlier in the startup process than if we were looking at the raw signal, reducing our chance of damaging the device.

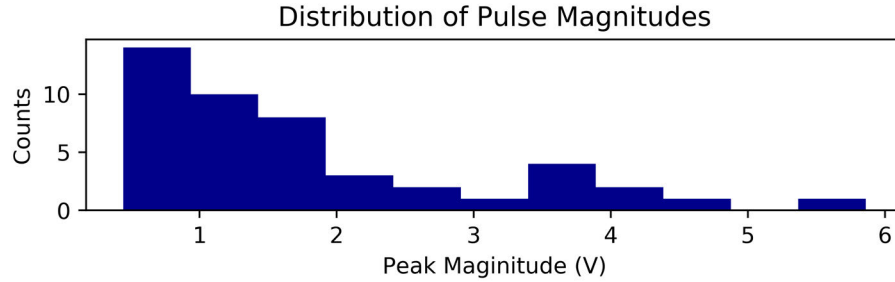


Figure 5.6: Histogram showing the number of pulses that reached specific heights.

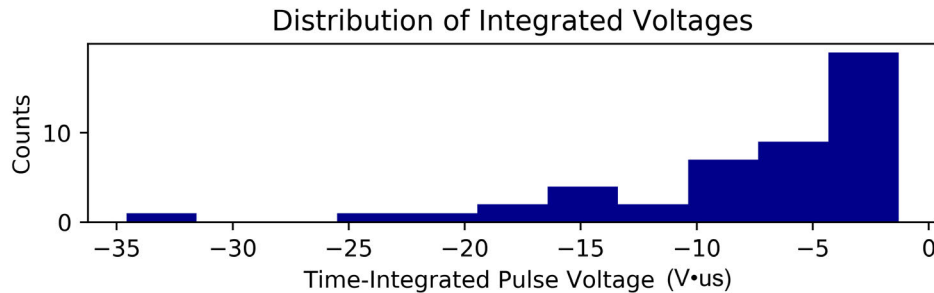


Figure 5.7: Distribution of the time-integrations of the pulse voltage. Note the stray signal is mostly low-energy, and thus should not affect data taken with larger sets of ions.

distribution of the time-integrals of the pulses, which can be found in 5.7. This histogram shows an analogue to the total current produced by the dark pulses (since the voltage is just an electron cascade measured through an impedance). This plot should be dominated by low values that would signal small, single particle incidents, since there is no consistent source of ions when nothing is in the chamber. As we see, this is the case. Having many incident particles at once, when we are producing ions, will show a larger magnitude of time-integrated voltage, since they will produce a higher total current upon hitting the MCP.

As a final way to test the MCP, we wanted to confirm that it could “see” particles originating at the ionization point. We could do this by searching for a signal prompted by scattered UV light. By triggering a scope off of the firing of the laser³

³Really, we triggered off the Q switch, an electro-optic modulator in the laser cavity. Normally,

without pulsing gas, we were able to see a consistently large signal on the MCP at a specific time after every pulse. Because the time was constant and there was no gas, it could not have been a signal due to ions, and we use it as evidence of the MCP picking up scattered UV light. This confirmed that the MCP has a line of sight to the ionization chamber, which should have been the case anyway. Nevertheless, this test allowed us to conclude our tests of the MCP, and to confirm that it was working properly.

5.4 Triggering

With the pressure characterized and the MCP operational, the last step in making the chamber operational was setting up the electrical triggering. Certainly, physical alignment is important to making sure the gas and laser pulses overlap, but temporal alignment is perhaps more so. Since the gas and light pulses travel at vastly different speeds, even perfect spatial alignment through the center of the ionization chamber will not produce ions if the pulses are displaced in space. As such, proper triggering of the two pulses is required to make sure they actually intersect.

The triggering cannot be done with a single pulse triggering both devices. The light pulse, though it travels down the laser table and back (through a dye laser and doubler), travels many times faster than the gas pulse, which travels ~ 470 m/s. If both were sent at the same time, the light would pass through the chamber before the tip of the gas pulse even made it a fraction of the way down the chamber. While we could conceivably use the output trigger on the laser to fire a gas pulse that a subsequent laser pulse could intersect, this requires a better time stability than the laser's internal clock offers.

As such, we decided to externally trigger both devices. To do so, we wrote a simple

the cavity does not build up a lot of power, but when the Q switch is on, power quickly builds up. To make the laser pulse, we turn on the Q-switch for a few nanoseconds. The YAG automatically sends out a voltage pulse when the switch is activated, which we could use for triggering.

program in Python which operated using the lab pulsing software. This program allows us to set and scan the time between pulses that trigger the gas and laser. We will begin the search for ionization with an estimate of what we believe should be the time between the two. To get such an estimate, we took several factors into account. First, of course, the difference in speed of the two beams. Since the molecular beam moves at hundreds of m/s rather than 3×10^8 m/s, the time between the firing of the laser and its arrival at the chamber is negligible compared to the molecular beam's traversal time. As such, the time between laser firing and arrival is taken to be zero. Accordingly, the major contributor to the time difference is the molecular beam's traversal time. The center of the chamber is located ~ 275 mm from the pulsed valve, giving a time of around 580-590 μs between when the valve opens and when the front of the beam makes it to the center. If we then send the light pulse 60 μs later, it will reach the chamber at approximately the same time as the middle of a 120 μs gas pulse. Therefore we will begin testing with 580-590 μs between when the gas and laser pulses are sent.

However, the laser electronics do not send a light pulse immediately on response of an external trigger. Instead, they trigger the flash lamp of the laser, which in turns triggers the release of the Q switch interlock at a set, but apparently not recorded in the manual, amount of time. By measuring the time difference between the input pulse and Q switch output trigger used above to observe the light on the MCP, we found that there is ~ 320 μs between the arrival of the trigger pulse and the exiting of the light. We subtracted this from the molecular traversal time to get an initial setting of 265 μs between the gas and laser trigger pulses. If we do not see ions with this setup, we can scan the time difference between pulses to find the best setting. The general order of the laser and gas fire pulses and the Q switch output trigger can be seen in Fig. 5.8, albeit with a shorter time between the pulses than what we will use. This profile also shows a fourth pulse, which is necessary to charge the laser

prior to firing.

5.5 Fully Operational

Though none of the processes were especially theoretically difficult to do, characterizing the gas moving through the chamber, testing the MCP, and creating a system of flexible electronic triggering are all vital to obtaining best use of the experimental vacuum chamber. Unfortunately, these were the last steps we completed within the timescale of this thesis. However, these tests have put us in good position to quickly move forward with finding and measuring the (2+1) REMPI process we seek to use in the $\dot{\mu}/\mu$ experiment.



Figure 5.8: Screenshot of an oscilloscope showing the timing of four pulses related to controlling the timing difference between the gas and light pulses. The horizontal timescale is $100 \mu\text{s}/\text{tick}$, and the vertical scales are shown in the bottom left. The red pulse is the one that releases the gas into the chamber. The blue pulse is sent to stimulate the laser to fire its flashlamps, and the short green pulse is a trigger showing when it actually does. Therefore, the timing between red and green is the time of interest, but the timing between red and blue is what we have control over. In this figure, that time is $\sim 170 \mu\text{s}$. During tests of the ionization, we will use a setting that make this time closer to $270 \mu\text{s}$ to temporally align the pulses. The yellow channel shows a pulse sent after a laser fires that begins a charging sequence for a subsequent light pulse. Note that the Q switch firing produces transients on the other channels. As such, it is possible to infer the time it fires without necessarily direct monitoring.

Chapter 6

Conclusion and Future Plans

Though we did not measure the photoionization spectrum we had hoped to by the end of this thesis, we reached a point where the path forward is clear to achieving this goal. Additionally, once we reach that point of demonstrated ionization, the main processes for implementing pieces of this chamber into the main laboratory apparatus are well understood. As a conclusion to this work, we use this chapter to discuss both the immediate and long-term plans for the project.

6.1 Short-Term

Two main obstacles stand in the way of using our operational chamber to observe O_2^+ REMPI and measure the photoionization spectrum. First, we will need to observe ionization in the first place. Then, we will need to make an automation system able to control the apparatus and measure the ionization spectrum. This second step is necessary because taking a smooth spectrum will require a larger number of data points than is possible to take reliably by hand, since each point requires a frequency adjustment and MCP signal measurement, neither of which is quick to do without automation. Though it is in some sense useful just by virtue of demonstrating REMPI, taking a spectrum will also tell us the beam temperature. Using this information,

we could optimize the beam for the μ/μ experiment by changing pulse time, gas pressure, or the delay between pulses. Overcoming each of these two obstacles is therefore conceptually straightforward but of great importance.

We are fairly certain that overlapping the oxygen gas and laser beams and achieving ionization is technically *possible* with our current setup. Nevertheless, there are a few tasks to complete before we observe it. At this time, we anticipate three main sources of difficulty between our current state of affairs and observing an ion signal on the MCP. First, actually getting the laser and gas beams to temporally overlap. Though we have a program that should be able to scan the time between the release of each pulse, we will need to interface the program electrically with the laser and actually scan the interval. We have tried to externally trigger the charging and firing of the laser with the program we developed, but the Q switch operated sporadically. Frequently, the laser did not produce a pulse when signaled. This seems solvable, but in either case needs to be looked at more. Second, we do not know the exact temperature of the beam, and so we do not know beforehand the frequency range that most ionization will occur in. This means we will need to be able to scan the laser over longer ranges. To do so, we will need to adjust the angle of the doubling crystal, and ideally automate the process to make it quick. Third, we do not know if we have put the ideal voltages on the accelerating lenses or on the MCP for optimal function, we only are matching the SimIon modelling. A poor configuration could result in bad focusing and ions missing the plate, and so we will have to optimize these values for the actual lab setup. Each of these steps is not especially difficult, but they all have to be done. Nevertheless, finding evidence of ionization should be fairly straightforward by scanning the parameter space of these variables in the coming weeks.

After some ionization is found, automating the chamber operation is also not a conceptually difficult process, but rather a matter of figuring out how to interface a range of technologies we use in the project. Specifically, we want to automate both

the frequency scanning and data collection process. For the frequency scanning, the difficulty lies in the fact that, as mentioned above, that scanning over a long range will require the crystal to be moved. Though it has a stepper motor setup to move it electronically, we have not explored how to make use of the motor and there is little information on how to use it. Nevertheless, it worked for Prof. Hunter, and so we should be able to figure it out. For data collection, we will need to record both the laser frequency and ion yield for each data point, and so both of these processes must be interfaced. Recording the laser frequency will be done by computerized monitoring of the pulsed wavemeter. Since the relevant figure for the MCP data is the integral of the recorded pulse, we will either record the integral as done by an oscilloscope, or record the pulse and integrate later. Both of these last steps will also require programs on the computer to actually save, keep track of, and analyze the data. None of these steps is difficult on their own, but they all still have to be done.

Though each of these larger obstacles is not trivial, we believe that we can at least observe photoionization within the next few weeks, and possibly begin to measure simple spectra within months. In any case, there are enough smaller tasks to occupy us until we are ready to integrate the time-of-flight electronics and MCP onto the main lab apparatus.

6.2 Longer-Term

As discussed in Chapter 2, we do plan to integrate two sections of the experimental chamber to the permanent vacuum chamber to use in the $\dot{\mu}/\mu$ measurement. Specifically, we will transfer both the molecular beam and time-of-flight apparatus. Though many of the pieces can be moved as-is, both systems also require additions to work with the ion trap.

Since ionizing out of a cold and dense beam can give us a relatively high number of

ground state O_2^+ ions compared to a room-temperature gas sample, we do want to use the beam as the molecular source on the $\dot{\mu}/\mu$ experiment. The assembly consisting of the mounted valve, pump, and skimmer on the four-way cross can likely be kept intact, perhaps with slight machining on the skimmer holding apparatus to better center the skimmer. However, in accordance with other groups that cool molecules out of a beam, we will likely need to add a second differentially pumped skimming section between the first skimmer and main chamber (e.g. [47]). This is because we need to maintain true UHV ($10^{-10} - 10^{-11}$ torr) around the ion trap; the background chamber pressure needs to be much below the $10^{-7} - 10^{-8}$ torr we observe in the temporary chamber. This addition can resemble the first skimming section, but will not need as large of a pump since the gas influx will be smaller. It may also be necessary to put the beam on a stage to more easily point it through the trap, but this would not change much of the structure. Therefore, although it will need additions, transferring the beam to the main lab chamber is fairly straightforward.

Moving the ion detection electronics will not be as simple. With more species of ions that we want to distinguish between (O_2^+ , O^+ , Be^+ , BeH^+ , among others), ion focusing will be more important, since missing a single ion could lead to false conclusions about what was in the trap. As such, we will need to add ion optics, electrostatic devices that act analogously to ions as normal lenses do to light, to the time-of-flight arm. To increase temporal, and therefore mass, resolution to distinguish between ionic species, we will also lengthen the TOF arm. We also need to figure out where to place the acceleration electrodes with respect to the trap, since their current spacing will not fit in the chamber. Though the plans so far discussed focus essentially on modifications of the apparatus we made in this project, we will also need genuine new methods to make the time-of-flight work with the ion trap. In particular, dumping the ions out of the trap is an extremely important, and yet touchy, process. Since the ions are not fully at rest in the trap due to micromotion,

instantly turning off the trap before accelerating may lead to altered time-of-flight distributions. Since they may be moving in different directions when first accelerated, two ions of the same species could arrive at the MCP at different times. Similarly for ions beginning at different points in the trap. Since our resolution needs to be very high, in such cases these particles could be identified incorrectly as different species. Working out details for this process must happen in conjunction with the addition of the existing apparatus to create a functional TOF arm. Though these processes will not necessarily be easy to work out, SimIon simulations and other experiments [48, 49] show that this integration of the time-of-flight system is possible, and so will not prevent us from reaching a point where $\dot{\mu}/\mu$ measurement can take place.

Though there is much to do, we thus see that moving from our current apparatus to an apparatus capable of measuring $\dot{\mu}/\mu$ is a relatively straight path. At this time, we are at a point where we understand (2+1) oxygen REMPI and have developed pieces of apparatus to create and measure ions with the process. Using relatively common tools in atomic, molecular, and optical physics such as supersonic beams, time-of-flight measurement, pulsed dye lasers, and a lot of electronics, we have enabled ourselves to state-selectively produce oxygen molecular ions. After fully realizing this process, we will move towards precisely measuring the frequency of the $v = 0 - 11$ vibrational transition in those ions. Long-term measurement of this quantity will provide us with one of two things, depending on the stability of the measurement. If we do not observe time variation, such data will provide proof-of-principle of narrow-linewidth oxygen molecular clocks, a model that will assist in continuing to develop human timekeeping. On the other hand, if the frequency, and therefore the proton-to-electron mass ratio, is seen to vary over time, we will have discovered a completely new phenomenon. In either case, we will use ions developed with the process and apparatus described in this work to advance the field of physics.

Appendix A

More Ionization Theory

The majority of relevant photoionization theory is discussed in Chapter 3. However, the details of how we were able to move from an infinite number of possible ionic states in the actual ionization to a finite set of products is more tedious, and as such is reproduced here for clarity of that chapter.

In our overview in Chapter 3, we were able to exclude some ionic states from the set of possible resultant states given a particular excited oxygen ion using only the propensities given by Xie and Zare [25]. This limit was given in terms of an equation dictating the allowed changes in angular momentum J . Reprinted here, we found that

$$\Delta J = l - \frac{1}{2} + 2n, \tag{A.1}$$

limited the possible ionization routes, where ΔJ is the change in total angular momentum, l is the orbital angular momentum removed by the exiting electron (allowed to be any odd integer), and n is any integer. This equation did not satisfy us, because ionization with off-resonant lasers has been done before, and such experiments seemed to produce ions in a finite number of states. While these experiments could have theoretically produced ions in an infinite set of states, their results show quite clearly that these possibilities are not equally probable. This is consistent with the

fact that we are not aware of further selection rules that dictate such an ionization *must* result in a finite number of ionic states. Thus, our quest to find a limit on the number of ionic states that will result from ionization of a molecular sample is simply a matter of determining which of the possible ionization routes are *most likely*.

As briefly introduced in Chapter 3, we do this by calculating the total dipole moment matrix element, expanded by Germann and Willitsch [40] for a Hund's case (b) \rightarrow case (b) ionization as,

$$P(J, J^+) = \sum_{l=0}^{\infty} \sum_{m_l=-l}^l \sum_{m_s=-s}^s \sum_{M_{J'}=-J'}^{J'} \sum_{M_{J^+}=-J^+}^{J^+} |\langle \eta^+, v^+, N^+ \Lambda^+ S^+ J^+ M_J^+ | \langle s m_s | \langle l m_l | \mu | \eta, v, N \Lambda S J M_J \rangle|^2 \quad (\text{A.2})$$

where N, Λ, S, J, M_J have their usual meanings, $s, m_s, l,$ and m_l are the quantum numbers for the photoelectron, v is the vibrational quantum number, and η is a placeholder for all additional quantum numbers needed to specify a particular state. Since our reaction is a (b) \rightarrow (a) transition instead of (b) \rightarrow (b), we need to change basis of the equation. We do this by inserting the identity operator that exchanges Ω^+ for N^+ (as Ω is a good quantum number for the ion, while N is not) into the modulus squared of matrix element:

$$\left| \sum \langle \Omega^+ | N^+ \rangle \langle n^+, v^+, N^+ \Lambda^+ S^+ J^+ M_J^+ | \langle s m_s | \langle l m_l | \mu | n, v, N \Lambda S J M_J \rangle \right|^2. \quad (\text{A.3})$$

Since the ion has $s = 1/2$, each state in a specified Ω^+ branch is a superposition of two N^+ states. Specifically in this case, the identity operator reduces the above equation to

$$|\alpha \langle N^+ = J^+ + \frac{1}{2} | \langle s m_s | \langle l m_l | \mu | N \rangle + \beta \langle N^+ = J^+ - \frac{1}{2} | \langle s m_s | \langle l m_l | \mu | N \rangle|^2, \quad (\text{A.4})$$

where the constants α and β are determined by Clebsch-Gordan coefficients. Since the matrix elements are allowed to be complex, this new formulation suggests there could be a phase dependence on the N makeup of the J^+ states. However, symbolic calculation shows that the phase mixing is negligible.

We do not have the expertise at this time to do full calculations of these elements. However, by simplifying the dipole moment matrix element into a collection of Wigner 3-, 6-, and 9-J symbols with a dependence on the spherical tensor matrix elements T'^k , as per Xie and Zare [25], we can observe certain trends. Helpful to this approach is the observation noted in [40] that

$$\langle n^+, v^+ | T'_0{}^k | n, v \rangle > \langle n^+, v^+ | T'_0{}^{k+1} | n, v \rangle. \quad (\text{A.5})$$

Here the prime on the spherical tensor simply designates that the calculation is in the coordinates of the molecule. The exact equations that interchange the dipole moment elements and spherical tensor elements are not especially helpful to see, but can be found in [40]. However, a byproduct of this process is that that only the spherical tensor elements involving $k = l \pm 1$ appear when rewriting the dipole matrix elements [40]. Since T'^k is expected to be vanishingly small for all $k > 2$, we infer that all $l > 3$ contribute minimally to the probability, in agreement with observed results [50].

With this knowledge in hand, Eqs. A.2 and A.4 provide a way to calculate the probability, in terms of spherical tensor elements, that a particular ionic state will be reached from an excited neutral state. The results of a sample calculation can be seen below in Table A.1 for the possible transitions when starting at $N'=2$. It is clear from this and similar calculations starting from different N' values that three likely values of ΔJ result in the ionization reaction. The strongest transition will be $\Delta J = +\frac{1}{2}$, with two weaker sidebands of $\Delta J = -\frac{3}{2}, +\frac{5}{2}$. Thus we expect 1-color photoionization (i.e. just using a single laser) to produce approximately six ionic states (the three

Table A.1: Table showing the possible ionic states resulting from ionization of the $J' = 2$ intermediate state. The probabilities in the Ω columns are in terms of spherical tensor matrix elements, with $A = T'^0$, $B = T'^2$. T'^4 and higher were assumed to be zero, as per observations of various other groups' calculations. Note there is a non-negligible probability of going from this state to the rovibrational ground state of the ion, $J^+ = \frac{1}{2}$. This is the strongest path to get to the ground state.

J'	J^+	$\Omega = \frac{1}{2}$	$\Omega = \frac{3}{2}$
2	$\frac{1}{2}$	$0.33B^2$	0
2	$\frac{5}{2}$	$0.33A^2 + 0.24B^2$	$0.67A^2 + 0.19B^2$
2	$\frac{9}{2}$	$0.32B^2$	$0.48B^2$
2	$\frac{13}{2}$	0	0

optional for ΔJ in each of the Ω branches) per intermediate state.

We have thus outlined how we managed to limit a potentially infinite number of possible resultant ionic states to a finite and well understood set of options. Though potentially infinite ionic states are technically possible results of the ionization, there are approximately six that are likely per intermediate state we ionize.

Bibliography

- [1] K. Higgins, D. Miner, C. Smith, and D. Sullivan, “A Walk Through Time,” (2004), URL <https://www.nist.gov/pml/walk-through-time-early-clocks>.
- [2] A. D. Ludlow, M. M. Boyd, J. Ye, E. Peik, and P. Schmidt, “Optical atomic clocks,” *Rev. Mod. Phys.* **87**, 637 (2015), URL <https://link.aps.org/doi/10.1103/RevModPhys.87.637>.
- [3] The ATLAS Collaboration, “Observation of a new particle in the search for the Standard Model Higgs boson with the ATLAS detector at the LHC,” *Physics Letters B* **716**, 1 (2012), ISSN 03702693, arXiv: 1207.7214, URL <http://arxiv.org/abs/1207.7214>.
- [4] The CMS Collaboration, “Observation of a new boson at a mass of 125 GeV with the CMS experiment at the LHC,” *Physics Letters B* **716**, 30 (2012), ISSN 03702693, arXiv: 1207.7235, URL <http://arxiv.org/abs/1207.7235>.
- [5] LIGO Scientific Collaboration and Virgo Collaboration, “Observation of Gravitational Waves from a Binary Black Hole Merger,” *Phys. Rev. Lett.* **116**, 061102 (2016), URL <https://link.aps.org/doi/10.1103/PhysRevLett.116.061102>.
- [6] M. S. Safronova, D. Budker, D. DeMille, D. F. J. Kimball, A. Derevianko, and C. W. Clark, “Search for New Physics with Atoms and Molecules,”

- arXiv:1710.01833 [hep-ph, physics:physics] (2017), arXiv: 1710.01833, URL <http://arxiv.org/abs/1710.01833>.
- [7] Y. V. Stadnik and V. V. Flambaum, “Can dark matter induce cosmological evolution of the fundamental constants of Nature?” *Physical Review Letters* **115** (2015), ISSN 0031-9007, 1079-7114, arXiv: 1503.08540, URL <http://arxiv.org/abs/1503.08540>.
- [8] D. Hanneke, R. A. Carollo, and D. A. Lane, “High sensitivity to variation in the proton-to-electron mass ratio in O_2^+ ,” *Physical Review A* **94** (2016), ISSN 2469-9926, 2469-9934, arXiv: 1607.06825, URL <http://arxiv.org/abs/1607.06825>.
- [9] G. Herzberg, *Molecular Spectra and Molecular Structure*, vol. Volume 1. Spectra of Diatomic Molecules (D.Van Nostrand Company Inc., 1989), reprint ed., ISBN 0-89464-270-7.
- [10] J. Brown and A. Carrington, *Rotational Spectroscopy of Diatomic Molecules* (Cambridge University Press, 2003), ISBN 0-521-53078-4.
- [11] A. Sur, C. V. Ramana, and S. D. Colson, “Optical spectra of the lowest Π_g Rydberg states in O_2 ,” *The Journal of Chemical Physics* **83**, 904 (1985), ISSN 0021-9606, URL <http://aip.scitation.org/doi/abs/10.1063/1.449506>.
- [12] A. Sur, R. S. Friedman, and P. J. Miller, “Rotational dependence of the Rydberg-valence interactions in the $^1\Pi_g$ states of molecular oxygen,” *The Journal of Chemical Physics* **94**, 1705 (1991), ISSN 0021-9606, URL <http://aip.scitation.org/doi/10.1063/1.459942>.
- [13] A. Dochain and X. Urbain, “Production of a rovibrationally selected O_2^+ beam for dissociative recombination studies,” *EPJ Web of Conferences* **84**, 05001 (2015), ISSN 2100-014X, URL <http://dx.doi.org/10.1051/epjconf/20158405001>.

- [14] J. Xie and R. N. Zare, “Selection rules for the photoionization of diatomic molecules,” *The Journal of Chemical Physics* **93**, 3033 (1990), ISSN 0021-9606, URL <http://aip.scitation.org/doi/abs/10.1063/1.458837>.
- [15] V. Letokhov, *Laser Photoionization Spectroscopy* (Elsevier, 1987).
- [16] G. Scoles, D. Bassi, U. Buck, and D. C. Laine, eds., *Atomic and Molecular Beam Methods: Volume 1* (Oxford University Press, New York, 1988), ISBN 978-0-19-504280-1.
- [17] H. Pauly, *Atom, Molecule, and Cluster Beams I: Basic Theory, Production and Detection of Thermal Energy Beams* (Springer, Berlin ; New York, 2000), 2000 edition ed., ISBN 978-3-540-66945-6.
- [18] B. Sawyer, *Cold polar molecules for novel collision experiments at low energies*, Ph.D. thesis, CU Boulder (2010).
- [19] J. L. Wiza, “Microchannel Plate Detectors,” *Nuclear Instruments and Methods* **162**, 587 (1979).
- [20] T. P. Heavner, E. A. Donley, F. Levi, G. Costanzo, T. E. Parker, J. H. Shirley, N. Ashby, S. Barlow, and S. R. Jefferts, “First accuracy evaluation of NIST-F2,” *Metrologia* **51**, 174 (2014), ISSN 0026-1394, URL <http://stacks.iop.org/0026-1394/51/i=3/a=174>.
- [21] D. DeMille, S. B. Cahn, D. Murphree, D. A. Rahmlow, and M. G. Kozlov, “Using Molecules to Measure Nuclear Spin-Dependent Parity Violation,” *Phys. Rev. Lett.* **100**, 023003 (2008), URL <https://link.aps.org/doi/10.1103/PhysRevLett.100.023003>.
- [22] E. J. Salumbides, J. C. J. Koelemeij, J. Komasa, K. Pachucki, K. S. E. Eikema, and W. Ubachs, “Bounds on fifth forces from precision measurements

- on molecules,” Phys. Rev. D **87**, 112008 (2013), URL <https://link.aps.org/doi/10.1103/PhysRevD.87.112008>.
- [23] S. Dimopoulos, P. W. Graham, J. M. Hogan, and M. A. Kasevich, “General Relativistic Effects in Atom Interferometry,” Physical Review D **78** (2008), ISSN 1550-7998, 1550-2368, arXiv: 0802.4098, URL <http://arxiv.org/abs/0802.4098>.
- [24] W. J. van der Zande, W. Koot, J. Los, and J. R. Peterson, “Predissociation of the $d\ ^1\Pi_g$ Rydberg state in O_2 : Nature of the Rydberg-valence interactions,” The Journal of Chemical Physics **89**, 6758 (1988), ISSN 0021-9606, URL <http://aip.scitation.org/doi/abs/10.1063/1.455350>.
- [25] J. Xie and R. N. Zare, “Rotational line strengths for the photoionization of diatomic molecules,” The Journal of Chemical Physics **97**, 2891 (1992), ISSN 0021-9606, URL <http://aip.scitation.org/doi/abs/10.1063/1.463030>.
- [26] J. A. Coxon and M. P. Haley, “Rotational analysis of the $A\ ^2\Pi_u \rightarrow X\ ^2\Pi_g$ second negative band system of $^{16}O_2^+$,” Journal of Molecular Spectroscopy **108**, 119 (1984), ISSN 0022-2852, URL <http://www.sciencedirect.com/science/article/pii/002228528490290X>.
- [27] W. Kong and J. W. Hepburn, “Rotationally resolved threshold photoelectron spectroscopy of O_2 using coherent XUV: formation of vibrationally excited ions in the Franck-Condon gap,” Can. J. Phys. **72**, 1284 (1994), ISSN 0008-4204, URL <http://www.nrcresearchpress.com/doi/abs/10.1139/p94-164>.
- [28] R. Ogorzalek Loo, W. J. Marinelli, P. L. Houston, S. Arepalli, J. R. Wiesenfeld, and R. W. Field, “Multiphoton ionization of O_2 X $^3\Sigma_g^-$, a $^1\Delta_g$, and b $^1\Sigma_g^+$ via the two-photon resonant $ns\sigma_g$, $nd\sigma_g$, and $nd\pi_g$ Rydberg levels,” The Jour-

- nal of Chemical Physics **91**, 5185 (1989), ISSN 0021-9606, URL <http://aip.scitation.org/doi/abs/10.1063/1.457589>.
- [29] M. Kajita, “Accuracy estimation of the $^{16}\text{O}_2^+$ transition frequencies targeting the search for the variation in the proton-electron mass ratio,” Phys. Rev. A **95**, 023418 (2017), URL <https://link.aps.org/doi/10.1103/PhysRevA.95.023418>.
- [30] M. Kajita, “Evaluation of variation in (m_p/m_e) from the frequency difference between the $^{15}\text{N}_2^+$ and ^{87}Sr transitions,” Applied Physics B: Lasers and Optics **122**, 203 (2016), ISSN 0946-2171, URL <http://adsabs.harvard.edu/abs/2016ApPhB.122..203K>.
- [31] H. Stoehr, F. Mensing, J. Helmcke, and U. Sterr, “Diode laser with 1 Hz linewidth,” Opt. Lett., OL **31**, 736 (2006), ISSN 1539-4794, URL <https://www.osapublishing.org/abstract.cfm?uri=ol-31-6-736>.
- [32] Y. N. Zhao, J. Zhang, A. Stejskal, T. Liu, V. Elman, Z. H. Lu, and L. J. Wang, “A vibration-insensitive optical cavity and absolute determination of its ultrahigh stability,” Opt. Express, OE **17**, 8970 (2009), ISSN 1094-4087, URL <https://www.osapublishing.org/abstract.cfm?uri=oe-17-11-8970>.
- [33] A. D. Ludlow, X. Huang, M. Notcutt, T. Zanon-Willette, S. M. Foreman, M. M. Boyd, S. Blatt, and J. Ye, “Compact, thermal-noise-limited optical cavity for diode laser stabilization at 1×10^{-15} ,” Opt. Lett., OL **32**, 641 (2007), ISSN 1539-4794, URL <https://www.osapublishing.org/abstract.cfm?uri=ol-32-6-641>.
- [34] L. Robertsson, S. Picard, F.-L. Hong, Y. Millerioux, P. Juncar, and L.-S. Ma, “International comparison of $^{127}\text{I}_2$ -stabilized frequency-doubled Nd:YAG lasers between the BIPM, the NRLM and the BNM-INM, October 2000,” Metrologia

- 38**, 567 (2001), ISSN 0026-1394, URL <http://stacks.iop.org/0026-1394/38/i=6/a=12>.
- [35] J. Ye, L. Robertsson, S. Picard, L.-S. Ma, and J. L. Hall, “Absolute frequency atlas of molecular I₂ lines at 532 nm,” *IEEE Transactions on Instrumentation and Measurement* **48**, 544 (1999), ISSN 0018-9456.
- [36] J. Ye, *Femtosecond Optical Frequency Comb* (Springer, 2005), URL www.springer.com/us/book/9780387237909.
- [37] S. R. Mackenzie, F. Merkt, E. J. Halse, and T. P. Softley, “Rotational state selectivity in N₂+X ²Σ_g⁺(ν⁺ = 0) by delayed pulsed field ionization spectroscopy via the a” ¹Σ_g⁺ (ν’= 0) state,” *Molecular Physics* **86**, 1283 (1995), ISSN 0026-8976, URL <http://dx.doi.org/10.1080/00268979500102731>.
- [38] S. T. Pratt, P. M. Dehmer, and J. L. Dehmer, “Resonant multiphoton ionization of H₂ via the B ¹Σ_u⁺, v = 7, J = 2 and 4 levels with photoelectron energy analysis,” *The Journal of Chemical Physics* **78**, 4315 (1983), ISSN 0021-9606, URL <http://aip.scitation.org/doi/abs/10.1063/1.445324>.
- [39] F. Merkt, R. Signorell, H. Palm, A. Osterwalder, and M. Sommariva, “Towards resolving the hyperfine structure in ions by photoelectron spectroscopy,” *Mol. Phys.* **95**, 1045 (1998), ISSN 0026-8976, URL <http://adsabs.harvard.edu/abs/1998MolPh..95.1045M>.
- [40] M. Germann and S. Willitsch, “Fine- and hyperfine-structure effects in molecular photoionization. I. General theory and direct photoionization,” *The Journal of Chemical Physics* **145**, 044314 (2016), ISSN 0021-9606, URL <http://aip.scitation.org/doi/10.1063/1.4955301>.
- [41] L. R. Hargreaves, J. R. Francis-Staite, T. M. Maddern, M. J. Brunger, and S. J. Buckman, “A new normalization method for electron collision cross sections

- measured using skimmed supersonic jet beams,” *Meas. Sci. Technol.* **18**, 2783 (2007), ISSN 0957-0233, URL <http://stacks.iop.org/0957-0233/18/i=9/a=007>.
- [42] E. R. Hudson, *Experiments on Cold Molecules Produced via Stark Deceleration*, Ph.D. thesis, University of Colorado, Boulder (2006).
- [43] L. A. Chewter, M. Sander, K. Müller-Dethlefs, and E. W. Schlag, “High resolution zero kinetic energy photoelectron spectroscopy of benzene and determination of the ionization potential,” *The Journal of Chemical Physics* **86**, 4737 (1987), ISSN 0021-9606, URL <https://aip.scitation.org/doi/abs/10.1063/1.452694>.
- [44] J. O’Hanlon, *A User’s Guide to Vacuum Technology* (Wiley, New York, 2005), 2nd ed.
- [45] Y. Song, M. Evans, C. Y. Ng, C.-W. Hsu, and G. K. Jarvis, “Rotationally resolved pulsed field ionization photoelectron bands of O_2^+ ($X^2\Pi_{1/2,3/2g}$, $v^+ = 0 - 38$) in the energy range of 12.05-18.15 eV,” *The Journal of Chemical Physics* **111**, 1905 (1999), ISSN 0021-9606, URL <http://aip.scitation.org/doi/abs/10.1063/1.479459>.
- [46] Jordan TOF Products, Inc., “Instruction Manual: 18mm MCP Microchannel Plate Detector,” URL <http://www.rmjordan.com/manuals/C701man.pdf>.
- [47] X. Tong, D. Wild, and S. Willitsch, “Collisional and radiative effects in the state-selective preparation of translationally cold molecular ions in ion traps,” *Physical Review A* **83**, 023415 (2011), ISSN 1050-2947, URL <http://adsabs.harvard.edu/abs/2011PhRvA..83b3415T>.
- [48] P. C. Schmid, J. Greenberg, M. I. Miller, K. Loeffler, and H. J. Lewandowski, “An ion trap time-of-flight mass spectrometer with high mass resolution

- for cold trapped ion experiments,” *Review of Scientific Instruments* **88**, 123107 (2017), ISSN 0034-6748, URL <http://aip.scitation.org/doi/full/10.1063/1.4996911>.
- [49] C. Schneider, S. J. Schowalter, P. Yu, and E. R. Hudson, “Electronics of an ion trap with integrated time-of-flight mass spectrometer,” *International Journal of Mass Spectrometry* **394**, 1 (2016), ISSN 1387-3806, URL <http://www.sciencedirect.com/science/article/pii/S1387380615003450>.
- [50] R. G. Tonkyn, J. W. Winniczek, and M. G. White, “Rotationally resolved photoionization of O_2^+ near threshold,” *Chemical Physics Letters* **164**, 137 (1989), ISSN 0009-2614, URL <http://www.sciencedirect.com/science/article/pii/0009261489850055>.